WATER RESOURCES RESEARCH, VOL. 45, W08436, doi:10.1029/2008WR007009, 2009

Interphase mass transfer in variable aperture fractures: Controlling parameters and proposed constitutive relationships

Russell L. Detwiler,[1] Harihar Rajaram,[2] and Robert J. Glass[3]

Received 19 March 2008; revised 15 December 2008; accepted 4 June 2009; published 27 August 2009.

[1] Interphase mass transfer in variable aperture fractures occurs in many problems where two immiscible fluids are present, such as dissolution of dense nonaqueous phase liquids into groundwater, dissolution of CO_2 in deep saline aquifers, and evaporation of trapped water by flowing gas during natural gas production. Typically, one fluid is entrapped by capillary forces and resides in immobilized regions whose distribution and geometry are controlled by the relative influence of capillary, gravitational, and viscous forces within the fracture. For the case of fractures bounded by a low porosity/permeability matrix, interphase mass transfer occurs predominantly owing to diffusive/advective transport from the entrapped phase interface into the phase flowing through the fracture. We explore the relative influence of the initial entrapped phase geometry and mean flowing phase velocities on the dissolution of the entrapped phase. Our systematic simulations use a percolation-based model of phase invasion and depth-averaged models of flow, transport, and mass transfer. The invasion model provides a physically based distribution of entrapped phase within the fracture and the mass transfer model implicitly calculates interphase mass transfer from discrete regions of entrapped phase without the need for empirical mass transfer relationships. Results demonstrate behavior across a wide range of initial entrapped phase distributions, with entrapped phase saturations ranging from zero to near the percolation threshold. Interfacial area evolves with a near-linear dependence on entrapped phase saturation during dissolution in each simulation, and fracture-scale intrinsic mass transfer rate coefficients exhibit a nonlinear dependence on Peclet number and a negligible dependence on entrapped phase saturation. These observations provide a basis for the development of constitutive relationships that quantify interphase mass transfer in variable aperture fractures as a function of entrapped phase saturation and flow rate; coarse-grid dissolution simulations using these constitutive relationships demonstrate good agreement with results from the high-resolution mechanistic simulations.

Citation: Detwiler, R. L., H. Rajaram, and R. J. Glass (2009), Interphase mass transfer in variable aperture fractures: Controlling parameters and proposed constitutive relationships, *Water Resour. Res.*, *45*, W08436, doi:10.1029/2008WR007009.

1. Introduction

[2] Mass transfer between two immiscible phases within fractures occurs in problems such as the dissolution of dense nonaqueous phase liquids (DNAPLs) into groundwater [e.g., *Kueper and Mcwhorter*, 1991; *Dickson and Thomson*, 2003], dissolution of CO_2 in deep saline aquifers [e.g., *Yang et al.*, 2005], and evaporation of trapped water by flowing gas during natural gas production [e.g., *Mahadevan et al.*, 2007]. Though these problems each pose unique challenges, they share fundamental processes that control interphase mass transfer rates. In each case, one phase flows through fractures that are partially occupied by a second immiscible phase, which is often entrapped by capillary forces. Interphase mass transfer occurs across the interfaces between the two fluid phases and is driven by advective and diffusive transport of the dissolving phase within the fracture. In addition, for fractures in porous and/or permeable rocks and clays, interphase mass transfer will occur across the interface adjacent to the matrix [e.g., *Parker et al.*, 1994; *O'Hara et al.*, 2000]. The relative magnitude of interphase mass transfer into the fracture versus the matrix will depend on the porosity/permeability of the matrix, flow rates through fractures and distribution of interfacial area within individual fractures. In this paper we focus on interphase mass transfer within the fracture, which will be dominant in rocks with low effective porosity such as granites and shales. In these cases, the distribution and geometry of entrapped phase regions will strongly influence transport in the flowing phase and thus mass transfer rates.

[3] Within individual fractures, the distribution and structure of the entrapped phase are controlled by the relative influence of capillary, gravitational, and viscous forces during the initial displacement process. Slow displacement into a horizontal fracture (i.e., negligible viscous and

---

[1] Department of Civil and Environmental Engineering, University of California, Irvine, California, USA.

[2] Department of Civil, Environmental, and Architectural Engineering, University of Colorado at Boulder, Boulder, Colorado, USA.

[3] Sandia National Laboratories, Albuquerque, New Mexico, USA.

Copyright 2009 by the American Geophysical Union.
0043-1397/09/2008WR007009$09.00

gravitational forces) results in an advancing interface that is controlled completely by capillary forces, which are proportional to the curvature of the interface. Two principal radii of curvature characterize interfacial curvature: out-of-plane curvature, which is controlled by surface wettability and the magnitude of the local aperture, and in-plane curvature, which is related to a characteristic length scale of aperture variability. The effect of out-of-plane curvature has been represented using standard invasion percolation models with invasion pressures inversely proportional to the local fracture aperture [*Chandler et al.*, 1982; *Wilkinson and Willemsen*, 1983]. However, this approach ignores the competing influence of in-plane curvature, which tends to smooth interfaces during invasion. *Glass et al.* [1998] showed that a modified invasion percolation (MIP) algorithm that accounts for in-plane curvature better represents experimental observations of immiscible fluid displacement in fractures. More recent MIP simulations of capillary-dominated invasions over a range of parameter space demonstrated the relative influence of in-plane and out-of-plane curvature and the wide range of possible entrapped phase structures and entrapped phase saturations [*Glass et al.*, 2003].

[4] In addition to the influence of capillary forces on phase displacement and entrapped phase distribution, pressure gradients within the invading/defending fluids, due to gravitational or viscous forces, can either stabilize or destabilize the advancing interface. A stabilizing gradient will reduce the amount of capillary-induced interfacial roughness and lead to decreased trapping during the displacement, whereas a destabilizing gradient will lead to development of fingers and substantially larger saturations of the entrapped phase [e.g., *Xu et al.*, 1998]. Clearly an effective model of interphase mass transfer must adequately account for a wide range of possible entrapped phase geometries.

[5] The complexity of local interphase mass transfer processes is usually lumped into bulk empirical parameters when quantifying mass transfer rates from experiments in columns of porous media [e.g., *Miller et al.*, 1990] or single fractures [*Dickson and Thomson*, 2003]. This is largely because measuring the distribution of the entrapped phase in these systems is difficult, not because small-scale processes are deemed unimportant. Efforts to quantify interfacial areas using light transmission in two-dimensional micromodels [e.g., *Detwiler et al.*, 2001; *Knutson et al.*, 2001] and X-ray computed microtomography in small cores [e.g., *Brusseau et al.*, 2008; *Culligan et al.*, 2006] have begun to provide insights into the connection between interfacial area and mass transfer rates. However, at the column or core scale, experiments are typically used to relate interphase mass transfer rates to the difference between some average aqueous phase concentration (c) of the dissolving phase and the equilibrium concentration (c_{eq}) [e.g., *Powers et al.*, 1994]:

$$V\frac{\partial c}{\partial x} = ka_i\left(c_{eq} - c\right) \qquad (1)$$

where V is the mean aqueous phase velocity, k (LT^{-1}) is an intrinsic mass transfer coefficient and a_i (L^{-1}) is the specific interfacial area between the two phases (interfacial area per volume of medium). Because it is difficult to quantify a_i in column or single fracture experiments, the product ka_i is often represented as a bulk mass transfer rate coefficient, K (T^{-1}), and calculated using experimental measurements of effluent concentration with the solution for (1) at the effluent end of the experimental systems (L) [e.g., *Powers et al.*, 1994]:

$$K = -\left(\frac{V}{L}\right)\ln\left(1 - \frac{c_{x=L}}{c_{eq}}\right) \qquad (2)$$

Estimates of K obtained from (2) provide a measure of the steady state mass transfer rate for the experiment that is implicitly tied to the distribution of the entrapped phase within the sample. Thus applying this model in different samples or at different scales requires that the distribution of the entrapped phase is similar. This may be reasonable in well-controlled laboratory experiments in homogeneous porous media, where an entrapped phase at residual saturation is likely to reside in small discrete ganglia occupying single to several pores [*Mayer and Miller*, 1996]. However, in variable aperture fractures [*Becker et al.*, 2003; *Detwiler et al.*, 2001; *Glass and Nicholl*, 1995] and two-dimensional micromodels [*Chomsurin and Werth*, 2003; *Jia et al.*, 1999; *Kennedy and Lennox*, 1997], the regions of entrapped phase have been shown to span a wide range of length scales and exhibit a range of morphologies depending on fluid and pore space properties and the forces acting during migration of the entrapped phase. In a previous study [*Glass et al.*, 2003], we carried out a detailed parametric study of capillary-driven invasions in variable aperture fractures using a modified invasion percolation (MIP) model that predicts observed experimental behavior quite well [*Glass et al.*, 1998]. The results demonstrated possible initial entrapped phase saturations that ranged from near the percolation threshold to zero depending on surface wettability, surface tension, aperture variability and spatial correlation. These results suggest potential challenges in extending mass transfer rates estimated from experiments in one fracture to different fractures and fluids, which may lead to widely varying entrapped phase structures and saturations. This motivates a detailed study of the influence of entrapped phase geometry on interphase mass transfer.

[6] To investigate the influence of entrapped phase morphology on interphase mass transfer, we use previously developed and tested computational models of phase invasion [*Glass et al.*, 1998] and entrapped phase dissolution [*Detwiler et al.*, 2001] to systematically investigate the relative influence of flow rate and a range of fracture and fluid properties as quantified by a set of dimensionless parameters. These mechanistic models explicitly represent the physics of fluid flow and mass transfer at the scale of individual blobs of entrapped phase, and thus require no empirical relationships to quantify mass transfer within the fracture. The results of parametric simulations carried out in synthetic aperture fields suggest that despite the wide range of spatial structure/morphologies of the dissolving entrapped phase, a set of constitutive relationships based upon the areal saturation of the entrapped phase, S_n, and Peclet number quantify transient dissolution rates from the fractures quite well. These relationships effectively represent the complexities of interphase mass transfer from a broad

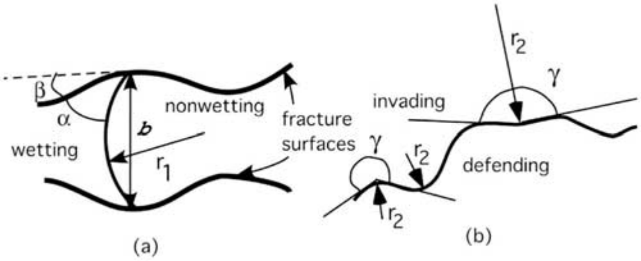

Figure 1. Schematic of two fluid phases within a rough-walled fracture: (a) Cross section defining the aperture-induced radius of curvature, r_1, local aperture, b, contact angle, α, and convergence/divergence angle, β. (b) Plan view (normal to fracture plane) defining the in-plane radius of curvature, r_2, and included angle γ (from invading phase).

range of geometries and hence can serve as a basis for representing mass transfer relationships in large individual fractures or networks of discrete fractures.

[7] The remainder of the paper is organized as follows: Section 2 presents an overview of the mechanistic model, including the MIP algorithm used for initial phase invasion and interface recession due to dissolution and the depth-averaged flow and transport algorithms. Section 3 details the computational interphase mass transfer experiments. Section 4 discusses the results from the computational experiments and introduces constitutive relationships for interfacial area, relative permeability and interphase mass transfer rates. Section 5 applies the constitutive models to coarse grid representations of the initial entrapped phase geometries used for the mechanistic simulations and compares results from the two modeling approaches. Section 6 provides concluding remarks.

2. Model Overview

[8] The simulations presented in this paper use two previously developed mechanistic computational models that have each been tested against experimental data. The first model uses the MIP approach to simulate migration of wetting/nonwetting fluids, where calculated local capillary pressures reflect both in-plane and out-of-plane curvature of fluid interfaces [*Glass et al.*, 1998]. The second model uses depth-averaged approximations of flow and transport equations within a fracture occupied by an entrapped, slowly dissolving phase. The dissolving phase is assumed to be at local equilibrium at the fluid-fluid interfaces, which leads to local mass transfer rates that are explicitly controlled by the geometry of the entrapped phase and the diffusive/advective transport of the dissolving phase [*Detwiler et al.*, 2001]. The assumption of local equilibrium at the fluid-fluid interfaces is widely accepted [e.g., *Dillard and Blunt*, 2000; *Knutson et al.*, 2001; *Pan et al.*, 2007] and reasonable when spatial resolution is sufficient to resolve individual regions of entrapped phase; it is the difficulty of explicitly representing interfaces in large-scale models that necessitates the use of mass transfer correlations. By explicitly representing the evolution of fluid-fluid interfaces and the resulting influence on flow, transport and local mass transfer, our modeling approach requires no empirical mass transfer correlations. Finally, the interface movements that accompany mass removal from entrapped regions can be computed explicitly using the MIP model. Thus in our approach, local interface movement is controlled by local capillary forces, which are treated rigorously at every interface segment of each entrapped blob, while mass transfer rates integrated over the entire interface of an entrapped blob constrain the rate of mass removal from each blob. In this section we present a brief overview of each of the models (refer to *Glass et al.* [1998] and *Detwiler et al.* [2001] for detailed descriptions of the phase invasion and dissolution models) and outline the scaling arguments [*Glass et al.*, 2003] that support our choice of parameters.

2.1. Phase Invasion/Recession

[9] The combination of capillary, gravitational, and viscous forces controls phase migration during invasion and the subsequent interface movement due to mass transfer from the entrapped phase into the flowing phase. In a gross sense, the nonwetting phase will reside in larger apertures and the wetting phase in smaller ones; however these tendencies are modified by connectivity between similar aperture values in the fracture resulting from a spatially correlated aperture field. *Glass et al.* [1998] used the Laplace-Young equation, which relates surface tension (τ) and interfacial curvature, as quantified by the two principal radii of curvature, r_1 and r_2, to the pressure jump across the curved interface (P_c) as the basis for the MIP algorithm for simulating invasion of immiscible fluids in variable aperture fractures:

$$P_c = -\tau\left(\frac{1}{r_1} + \frac{1}{r_2}\right) \tag{3}$$

[10] In equation (3), r_1 is measured normal to the plane of the fracture and r_2 is measured in the fracture plane (Figure 1). *Glass et al.* [1998] defined

$$r_1 = \frac{-b}{2\cos(\alpha + \beta)}$$

$$r_2 = \langle r_2 \rangle \tan\left(\frac{\gamma}{2}\right)$$

where b is the local aperture, α is the fluid/fluid/solid contact angle, β is the convergence/divergence angle of the fracture surfaces, $\langle r_2 \rangle$, is the mean in-plane radius of curvature, which is estimated as $\lambda/2$, where λ is the correlation length of the aperture field, and γ is a weighted measure of the local included angle of the interface. Substituting these expressions for r_1 and r_2 into (3) results in the following:

$$P_c = \tau\left(\frac{-2\cos(\alpha + \beta)}{b} + \frac{2}{\lambda}\cot\left(\frac{\gamma}{2}\right)\right) \tag{4}$$

[11] We simplify our analysis by assuming that convergence/divergence angles are small and the invading fluid is nearly perfectly wetting or nonwetting (i.e., $\alpha \approx 0$ or π). We then incorporate (4) into a more general invasion percolation algorithm by including terms for gravitational forces [e.g., *Glass and Yarrington*, 2003] and a first-order approx-

imation to viscous forces [e.g., *Xu et al.*, 1998] for calculating local invasion pressures:

$$P_{inv} = \tau\left(\frac{-2(\cos\alpha)}{b} + \frac{2}{\lambda}\cot\left(\frac{\gamma}{2}\right)\right) - \Delta\rho g x\cos\theta + \frac{V}{kk_r}\mu_{inv}(1 - Mk_r)x \qquad (5)$$

where subscripts "*inv*" and "*def*" represent the invading and defending fluids, respectively, x is the distance from the fracture inlet to the invading interface, $\Delta\rho = \rho_{inv} - \rho_{def}$, θ is the angle between the mean fracture plane and the gravitational vector, V is a mean velocity of the displacement front, μ_{inv} is the viscosity of the invading fluid, $M = \mu_{def}/\mu_{inv}$, is the mobility ratio, and k and k_r are estimates of the permeability of the fracture and the relative permeability between the invading interface and the fracture inlet. The second and third terms on the right-hand side of (5) reflect the influence of gravity and viscous forces on local movements of the invading interface; the sign and relative magnitude of these terms determines whether the displacement is stable or unstable.

[12] To facilitate design of parametric investigations of the role of entrapped phase structure on flow, transport, and interphase mass transfer, *Glass et al.* [2003] derived a dimensionless equation describing perturbations (P'_c) of P_c along the advancing interface. We extend that analysis to include the influence of gravitational and viscous forces on perturbations in P_{inv}

$$P'^{*}_{inv} = \mp\delta b'^{*} + C\cot\left(\frac{\gamma}{2}\right) + Gx^{*} \qquad (6)$$

where

$$P'^{*}_{inv} = \frac{\langle b\rangle}{2T}P'_c \quad b'^{*} = \frac{b'}{\sigma_b} \quad \delta = \frac{\sigma_b}{\langle b\rangle} \quad C = \frac{\langle b\rangle}{\lambda} \quad x^{*} = \frac{x}{\Delta x}$$

$$G = (Ca(1 - Mk_r) - Bo) \quad Ca = \frac{V\mu_{inv}\langle b\rangle\Delta x}{2kk_r\tau} \quad Bo = \frac{\langle b\rangle\Delta x\Delta\rho g\cos\theta}{2\tau}$$

In the above definitions, $\langle b\rangle$ and σ_b are the mean and standard deviation of the aperture field and b' is the local perturbation from the mean aperture. C is the dimensionless curvature number, which weighs the mean influence of in-plane curvature versus aperture-induced curvature on capillary forces and G is a dimensionless linear gradient that approximates the influence of viscous and gravitational forces as quantified by the capillary number (Ca) and Bond number (Bo), respectively. Thus, it is the relative magnitudes of G and C, which each represent a range of possible values of their defining dimensional parameters, that control the geometry of an advancing interface. Negative values of G reduce the impact of perturbations along the interface, leading to decreased trapping, and positive values of G enhance perturbations along the interface leading to instabilities and fingering. Note that δ is the coefficient of variation of the aperture field, which controls the roughening of an advancing interface by local aperture variations. For a given value of G, any values of $\langle b\rangle$, σ_b, and λ that yield the same value of C/δ, will yield similar entrapped phase structures. Wetting and nonwetting invasion simulations on multiple aperture field realizations with different values of δ support this scaling argument [*Glass et al.*, 2003]. In this paper, we consider a broad range of phase structures that span a range of C/δ and include a range of negative values of G.

2.2. Mass Transfer

[13] Viscous flow through a variable aperture fracture can be approximated by the two-dimensional Reynolds equation

$$\nabla\cdot(b\mathbf{v}) = 0 \qquad (7)$$

where b is the local aperture and the average flow velocity is given by

$$\mathbf{v} = -\frac{b^2 g}{12\nu}\nabla h \qquad (8)$$

where ν is the kinematic viscosity of the flowing fluid, h is the local pressure head, and g represents acceleration due to gravity. In a fracture occupied by two phases, (8) can be used to calculate the pressure field in the flowing phase, with the boundary conditions

$$\nabla h\cdot\mathbf{n} = 0 \qquad (9)$$

along fluid-fluid interfaces, where $\mathbf{n}$ is the unit vector normal to the interface. Note that in the numerical implementation of this model, one phase or the other occupies each grid block. This assumes that the nonwetting phase completely spans the fracture aperture and neglects flow through thin wetting phase films between the fracture surface and the nonwetting phase. Flow through thin films on fracture surfaces can be significant under certain conditions in partially saturated, fractured porous rocks [e.g., *Tokunaga and Wan*, 1997]. However, in a fracture filled with two aperture-spanning fluids with isolated regions of entrapped nonwetting phase, the wetting phase will be adsorbed predominantly to the surfaces in very thin films and held in small (relative to the size of entrapped blobs) depressions in the surface by the added influence of capillary forces [e.g., *Or and Tuller*, 2000]. These films will be at least an order of magnitude thinner than the fracture apertures (with transmivity about 3 orders of magnitude smaller than regions occupied solely by the flowing phase). Thus, the films will be relatively stagnant, and any mass transfer into the films will quickly cause the concentration of the dissolving phase in the films to reach equilibrium, inhibiting further mass transfer.

[14] As discussed by *Detwiler et al.* [2001], integrating the three-dimensional Stokes equations across the aperture precludes specifying momentum transfer across fluid-fluid interfaces. Because momentum transfer between the fluids will influence velocities in the immediate vicinity of the fluid-fluid interfaces, the simplified model may overestimate velocities in a thin (O(b)) boundary layer adjacent to entrapped regions. The magnitude of the resulting errors in the depth-averaged velocities will depend on the relative viscosities of the entrapped and flowing fluids and for most cases, the influence on mass transfer rates is small (see Appendix A).

[15] Mass transfer between the entrapped phase and the flowing phase is controlled by advective and diffusive mass

transport within the flowing phase. The two-dimensional advection-diffusion equation provides an estimate of the steady state distribution of mass within the flowing phase:

$$\nabla \cdot (b\mathbf{v}c) = \nabla \cdot (b\mathbf{D}_m \cdot \nabla c) \tag{10a}$$

where c is the depth-averaged concentration (note that lowercase c denotes dissolved concentration and uppercase C denotes curvature number), and D_m is the molecular diffusion coefficient of the entrapped phase in the flowing phase. Equation (10a) assumes molecular diffusion provides the dominant mixing mechanism and does not explicitly account for dispersion caused by velocity variations either in the fracture plane or across the aperture. By specifying adequately fine grid spacing, dispersion caused by in-plane velocity variability is accounted for implicitly. A sensitivity analysis demonstrated that the out-of-plane velocity variations that result in Taylor dispersion do not significantly influence simulation results [*Detwiler et al.*, 2001] over the range of Peclet numbers considered in this study, which also supports neglecting dispersion in (1). The boundary condition for (10) at fluid-fluid interfaces is that $c = c_s$, the solubility limit of the entrapped fluid in the flowing fluid, corresponding to a condition of local equilibrium. Local interphase mass fluxes between the entrapped phase and flowing phase are calculated as

$$j = D_m \nabla c \cdot \mathbf{n} \tag{10b}$$

along the entire length of each interface, and the concentration in the flowing phase at the interface is the equilibrium concentration of the entrapped phase in the flowing phase.

[16] Equation (10a) can be nondimensionalized to yield

$$\nabla \cdot (\mathbf{v}'c') = \frac{1}{Pe}\nabla \cdot b'\nabla c'$$

$$b' = \frac{b}{\langle b \rangle} \quad x' = \frac{x}{\langle b \rangle} \quad y' = \frac{y}{\langle b \rangle} \quad c' = \frac{c}{c_s} \quad \mathbf{v}' = \frac{\mathbf{v}}{\langle \mathbf{v} \rangle} \quad Pe = \frac{\langle |\mathbf{v}| \rangle \langle b \rangle}{D_m} \tag{11}$$

so that Pe provides a single parameter for quantifying the relative magnitudes of advective and diffusive transport during simulations. Equation (11) uses the depth-averaged concentration gradients adjacent to the fluid-fluid interface to drive mass transfer. Thus, this approach ignores concentration gradients across the fracture aperture. In Appendix A, we demonstrate that approximating mass transfer by using depth-averaged velocities and concentrations is well justified.

[17] Mass transfer from individual entrapped regions results in shrinkage of these regions and associated interface movement that follows (6); that is, the interface of any entrapped region recedes first from locations where P_c is smallest. Thus, capillary/gravity/viscous forces along each interface control interface movement and mass transfer rates are controlled by mass transport in the flowing fluid. Fracture-integrated mass transfer fluxes (J) are quantified by integrating (11) over all interfaces within the fracture at any time (t)

$$J = \rho_{def}\frac{V_f}{A_i}\frac{\partial S}{\partial t} = \frac{1}{A_i}\int_{A_i} j\,du \tag{12a}$$

where A_i is the total interfacial area and V_f is the volume of the fracture. Mass transfer rates are often expressed in terms of the dimensionless Sherwood number (Sh), which is defined as

$$Sh = \frac{Jl}{c_s D_m} \tag{12b}$$

where l is a characteristic length scale for mass transfer. In studies of porous media, mean grain diameter is often used as a characteristic length scale because it is closely related to the mean pore diameter, and residual entrapped nonaqueous phase is often trapped as isolated blobs in individual pores [e.g., *Mayer and Miller*, 1996]. In fractures, $\langle b \rangle$ is the analogous characteristic length scale [e.g., *Dickson and Thomson*, 2003] and is useful because it is a constant property of a given fracture. We adopt this convention here, but we note that, in fractures, entrapped regions of nonaqueous phase, and the distances between these regions, span multiple length scales that are dependent on C/δ and G, challenging our ability to define a unique mass transfer length scale.

[18] The approach for modeling mass transfer described by equations (10)–(12) assumes that mass transfer only occurs orthogonal to interfaces where they span the fracture aperture. Thus, thin films between the entrapped phase and the rock surfaces are neglected. As discussed in section 2.2, flow through these thin films is expected to be negligibly small, so, for the case of a low-porosity medium (i.e., negligible matrix diffusion) as presented here, concentrations of the dissolving entrapped phase in these films will quickly reach equilibrium. Because the fluid in the films is relatively stagnant, mass transfer into the films will not contribute significantly to dissolution. This was confirmed by excellent agreement between experiment and simulation [*Detwiler et al.*, 2001]. However, in a porous rock or clay, where diffusion into the matrix is significant [e.g., *O'Hara et al.*, 2000; *Parker et al.*, 1997], it is clear that accounting for the interfacial area within thin films and the resulting diffusion into the matrix will be important. Some pore network models of mass transfer and dissolution, invoke film flow along the corners of pores to improve agreement between experimental observations and simulations [*Dillard and Blunt*, 2000]. This is necessary because the entrapped phase typically resides in the pore bodies and without film flow, mass transfer would be controlled completely by diffusion through the neighboring pore throats. However, in fractures, advection immediately adjacent to aperture spanning interfaces is explicitly represented and leads to significant mass transfer from these regions [*Detwiler et al.*, 2001].

[19] Evaluation of the coupled model described in this section by detailed comparison to quantitative experiments [*Detwiler et al.*, 2001] demonstrated that this mechanistic modeling approach accurately predicts both the evolving spatial distribution of a dissolving entrapped phase, and the long-term mass transfer rates over the duration of a DNAPL dissolution experiment. This supports the use of the above modeling approach for a detailed evaluation of the role of entrapped phase structure and flow rates on interphase mass transfer processes.

3. Computational Experiments

[20] We designed a series of systematic computational experiments to investigate the influence of C/δ, G, and Pe_o

(initial Peclet number = $V_o\langle b\rangle/D_m$) in synthetic correlated random aperture fields. On the basis of a model proposed by *Brown* [1995] to describe two-dimensional fracture aperture fields, we defined a power spectrum for aperture variations of the form

$$\xi(\mathbf{k}) \propto \left(1 + \mathbf{l}^2|\mathbf{k}|^2\right)^{-\left(\frac{1}{2}+H\right)} \tag{13}$$

where $\mathbf{k}$ is the wave number vector, H is the Hurst exponent, which is typically in the range $0.5 < H < 1$, and l is a cutoff length scale. This functional form of $\xi(\mathbf{k})$ yields a smooth transition from the power law behavior ($\mathbf{k} > 1/l$) to the cutoff value ($\mathbf{k} < 1/l$) that results in random fields with well-behaved semivariograms (i.e., no oscillations as occur with an abrupt cutoff). The cutoff value reflects the length scale above which the two fracture surfaces are well matched. We generated a 1024 × 2048 correlated random aperture field with $H = 0.8$, $\langle b\rangle = 0.02$ cm, $\sigma_b = 0.005$ cm, grid spacing of 0.015 cm, and a correlation length, $\lambda = 0.075$ cm (defined as the separation distance at which the semivariogram reached a value of $\sigma^2(1-1/e)$). The values of these parameters all fall within the range reported by *Brown* [1995] for apertures resulting from a range of different fracture surfaces. We simulated dissolution in this baseline aperture field using a broad range of parameters ($C/\delta = 0$, 0.5, 1, 2, and 4; $Pe_o = 0.4$, 2, 10, 50, and 250; $G = 0.0$, -0.25 and -1.0) to quantify the relative influence of each of the relevant parameters.

[21] We then chose a subset of parameters ($C/\delta = 0$, 0.5, 1, 2; $Pe_o = 0.4$, 10, 250, $G = 0$) to investigate the influence of variations between aperture field realizations on simulated mass transfer rates in 5 additional aperture fields with identical statistics ($\langle b\rangle$, σ_b and λ) to the baseline fracture. These additional simulations provide a qualitative check of the relative (systematic) influence of the varied parameters (C/δ, Pe, and G) versus interrealization variability. Specifically, if we are to contend that any attribute related to mass transfer exhibits a systematic dependence on C/δ, and/or Pe, and/or G, the systematic variations of that attribute should be significantly larger than interrealization variability of the same.

[22] The resulting 135 simulations were run using the following procedure: The fractures were initially fully saturated with a nonwetting, nonaqueous phase and subsequently invaded by a wetting, aqueous phase along one of the short edges. The nonwetting phase was free to flow from the remaining three edges of the fracture. This configuration represents likely scenarios in different physical systems of interest such as pooling of DNAPL above relatively low permeability regions or pooling of CO_2 beneath impermeable cap rocks. In both of these scenarios, once the nonwetting fluid encounters a low-permeability barrier, it will begin to displace the resident fluid from fractures through a gravitationally stable displacement process leaving only small amounts of residual wetting phase in the smallest aperture regions. Subsequent redistribution of the phases may result when the pressure in the nonwetting fluid exceeds the entry pressure of the barrier or the nonwetting phase breaks through the low- permeability barrier, resulting in imbibition of the wetting phase similar to that represented by our invasion simulations. We acknowledge that there are other possible phase displacement scenarios that will lead to different configurations of the entrapped phase and the possibility of different mass transfer characteristics. The influence of the initial displacement processes on phase structure and subsequent mass transfer rates is an area for future study. We assume that during the relatively rapid (relative to interphase mass transfer rates) quasi-static displacement process, interphase mass transfer was negligible. We then initiated the mass transfer simulations by specifying a constant pressure gradient across the length of the fracture, no-flow boundaries along the sides (long edges) and an influent concentration of dissolved nonwetting phase, $c_{x=0} = 0$ and ran each simulation until S decreased to zero.

4. Results

[23] The mechanistic mass transfer and dissolution model used for this study provides the unique opportunity to directly calculate spatially variable local mass transfer rates across all NAPL-water interfaces, and their influence on evolving entrapped phase structure. This ability to quantify the influence of local processes on the fracture-scale behavior allows us to evaluate the utility of simplified constitutive models for predicting nonaqueous phase dissolution from variable aperture fractures over a wider range of parameter space than is feasible experimentally. In this section, we present results from the parametric dissolution simulations and propose constitutive relationships that effectively relate flow and mass transfer rates to entrapped phase saturation and flow rate.

4.1. Initial Conditions

4.1.1. Entrapped Phase Distribution and Saturation

[24] Figure 2 shows the entrapped nonwetting phase distributions after completion of the wetting phase invasion, superimposed on the fracture aperture field for $C/\delta = 0$, 0.54 and 1 and $G = 0$ and -1. Note that the case of $C/\delta = 0$ represents the limit of zero in-plane curvature such that the order of interface displacements is determined completely by the magnitudes of local apertures (as in standard invasion percolation) and the case of $G = 0$ corresponds to displacements driven solely by capillary forces. As C/δ increases, the influence of in-plane curvature on the invasion process increases, resulting in more compact entrapped regions with smoother interfaces. Although not immediately evident from Figure 2, the size of individual entrapped regions is larger for smaller C/δ. At $C/\delta = 0$, the entrapped regions have highly contorted (and less compact) shapes, with numerous thin "necks" providing continuity of the entrapped areas. For $C/\delta = 0$, there is typically one large entrapped region that spans almost the entire width of the fracture. Decreasing the value of G reduces trapping along the advancing interface during invasion, leading to smaller, more uniformly sized entrapped regions. Wetting fluid invasion into the fracture results in a wide range of initial nonaqueous phase saturations (S_{no}) that show a strong dependence on both C/δ and G. Here we define the nonaqueous phase saturation (S_n) as the areal saturation, or the fraction of the fracture area occupied by the nonaqueous phase. This is directly related to S, the volumetric saturation by $S_n = S\ \langle b\rangle/\langle b_n\rangle$, where $\langle b_n\rangle$ is the mean aperture for the portion of the fracture occupied by the

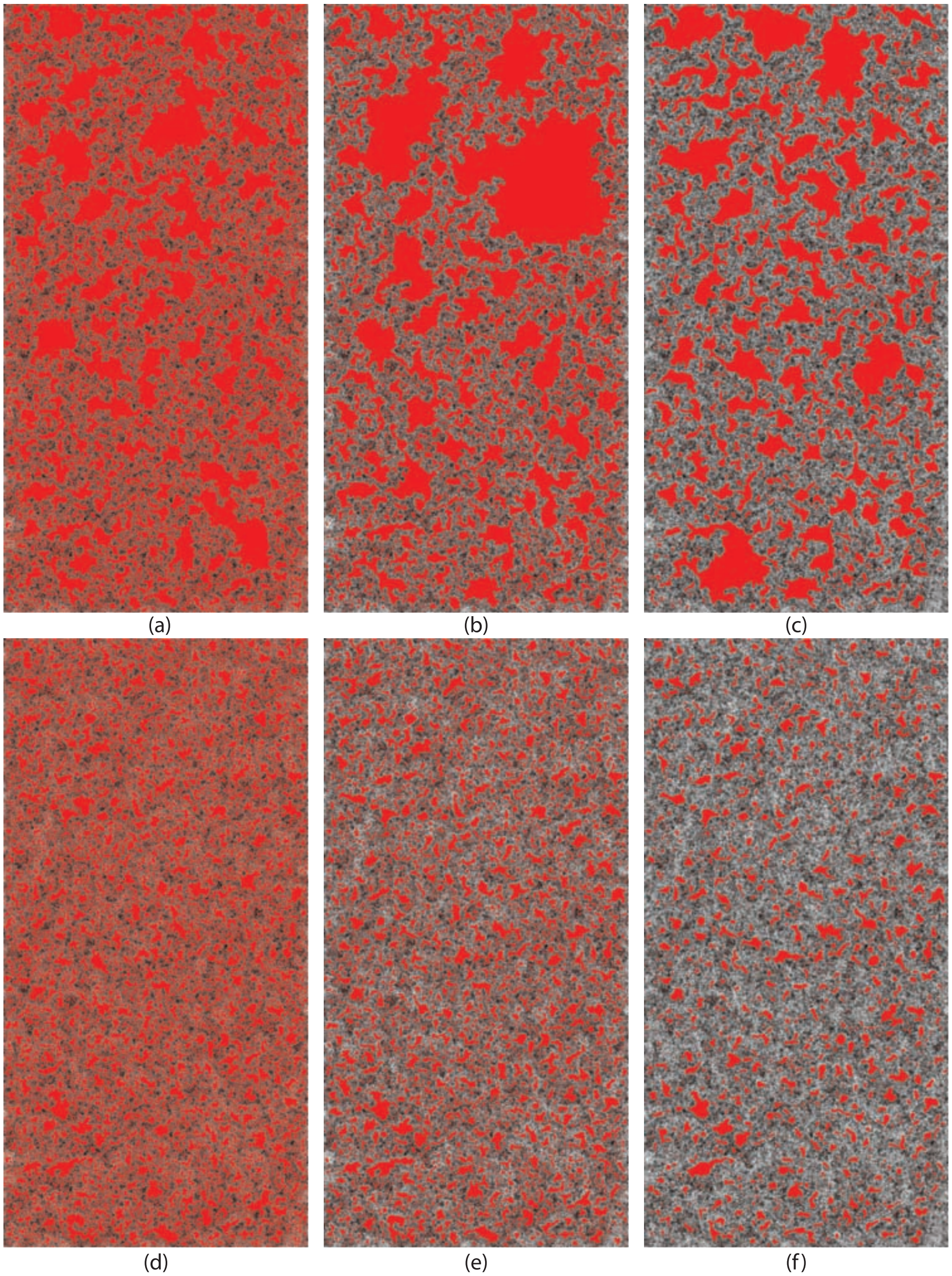

Figure 2. Examples of initial entrapped phase structure (red) superimposed on the baseline fracture aperture field. The gray scale represents apertures increasing from 0 to 0.04 cm (black to white). Parameter values are (a) $C/\delta = 0$, $G = 0$, $S_{no} = 0.62$; (b) $C/\delta = 0.54$, $G = 0$, $S_{no} = 0.52$; (c) $C/\delta = 1.1$, $G = 0$, $S_{no} = 0.35$; (d) $C/\delta = 0$, $G = -1.0$, $S_{no} = 0.51$; (e) $C/\delta = 0.54$, $G = -1.0$, $S_{no} = 0.32$; and (f) $C/\delta = 1.1$, $G = -1.0$, $S_{no} = 0.15$. The $C/\delta = 0$ cases represent standard invasion percolation simulations, and increasing values of C/δ represent the increasing influence of in-plane curvature. Flow of the invading (flowing) phase was from top to bottom.

nonaqueous phase. Figure 3 shows S_{no} plotted against C/δ for each of the values of G. The initial nonaqueous phase saturation (S_{no}) decreases with C/δ for all values of G, owing to the role of in-plane curvature in smoothing an advancing interface [*Glass et al.*, 2003]. Smaller values of G result in a reduction in the size of entrapped regions and a corresponding decrease in S_{no} for all values of C/δ. Note that experimental measurements of residual DNAPL saturation (21–27%) in two horizontal ($G = 0$) natural limestone fractures [*Longino and Kueper*, 1999] fall between the calculated values of S_{no} for C/δ = 1.1 and 2.2. Though *Longino and Kueper* [1999] did not report measurements of aperture field statistics, these values of C/δ are representative of values obtained from measurements of natural fractures in different rock types [*Brown*, 1995].

4.1.2. Interfacial Area

[25] The interfacial area between the entrapped and flowing phases is expected to influence mass transfer rates

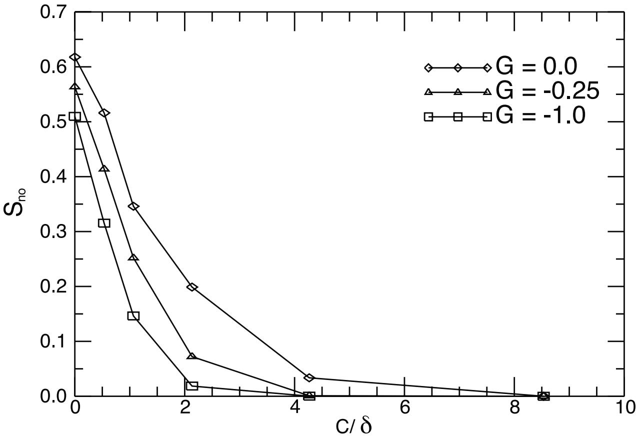

Figure 3. Initial values of areal saturation (S_{no}) at end of invasion stage of simulations for $G = 0.0$ (diamonds), -0.25 (triangles) and -1.0 (squares). In addition to reducing the sizes of the entrapped structures, increasing the magnitude of G leads to a reduction in S_n.

from the entrapped nonaqueous phase. We define an intrinsic interfacial area, $a_i = A_i/V_f$. Figure 4 shows the initial intrinsic interfacial area a_{io} plotted against S_{no} for the three values of G and demonstrates power law scaling of a_{io} with S_{no} and a secondary dependence on G. This behavior can be approximated well by a relationship of the form

$$a_{io} = \alpha' S_{no}^{1+\exp(-\beta'|G|)} \tag{14}$$

where α' and β' are fitted parameters. Note that for the case of $G = 0$, a_{io} is proportional to S_{no}^2. For the range of parameter space presented here, $\alpha' = 60$ cm^{-1} and $\beta' = 2.4$ fit the data well, as demonstrated by the fitted curves in Figure 4. We note that the values of α' and β' are specific to the invasion process used for our study, but it is likely that a_{io} will exhibit similar power law scaling in different configurations, though this remains to be investigated. For the $G = 0.0$ results, the data points represent the average of the 6 realizations, and the error bars reflect one standard deviation. These results demonstrate that the intrinsic interfacial area is insensitive to interrealization variability, and that there is a systematic dependence of a_{io} on the parameters C/δ and G controlling the entrapped phase structure.

4.2. Entrapped Phase Dissolution

[26] Gradients of the dissolved nonaqueous phase concentrations in the vicinity of the water/nonaqueous phase interfaces drive local mass transfer. The relative rates of advection and diffusion of dissolved nonaqueous phase, the morphology and spatial distribution of the entrapped regions, and the interface area between the fluids in turn control these concentration gradients. We expect that for a given hydraulic gradient, mass transfer will be more efficient for initial saturation fields where the individual entrapped regions are smaller and more uniformly distributed (i.e., large C/δ or $G < 0$) than in fields dominated by large, tortuous entrapped regions (i.e., small C/δ and $G \approx 0$). Large tortuous entrapped regions significantly reduce relative permeability (and thus flow through the fracture) and limit the fraction of interfaces between the flowing and entrapped phase that are adjacent to active flow paths. Thus, it is reasonable to expect that the wide range of initial entrapped phase distributions represented in Figure 2 will yield significant differences in dissolution behavior over the range of C/δ and G.

4.2.1. Evolution of Saturation Profiles

[27] It is instructive to quantify the entrapped phase saturation and dissolved nonaqueous phase concentrations

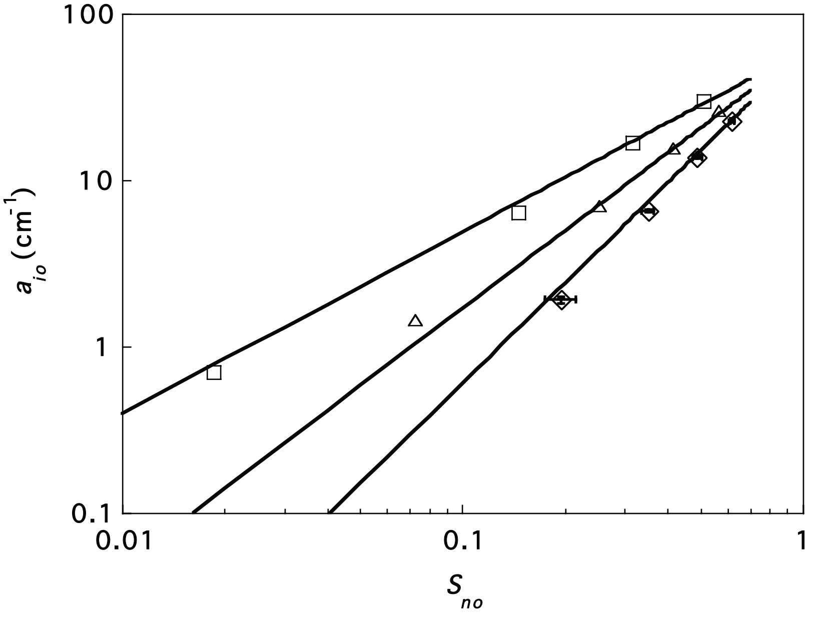

Figure 4. Initial specific interfacial area ($a_{io} = A_i/V_f$) plotted against initial entrapped phase saturation (S_{no}). Error bars for $G = 0$ case represent 1 standard deviation of the values obtained for five additional realizations. The lines represent the best fit of the power law relationship $a_{io} = \alpha' S_{no}^{1+\exp(-\beta'|G|)}$ with parameter values of $\alpha' = 60$ cm^{-1} and $\beta' = 2.4$.

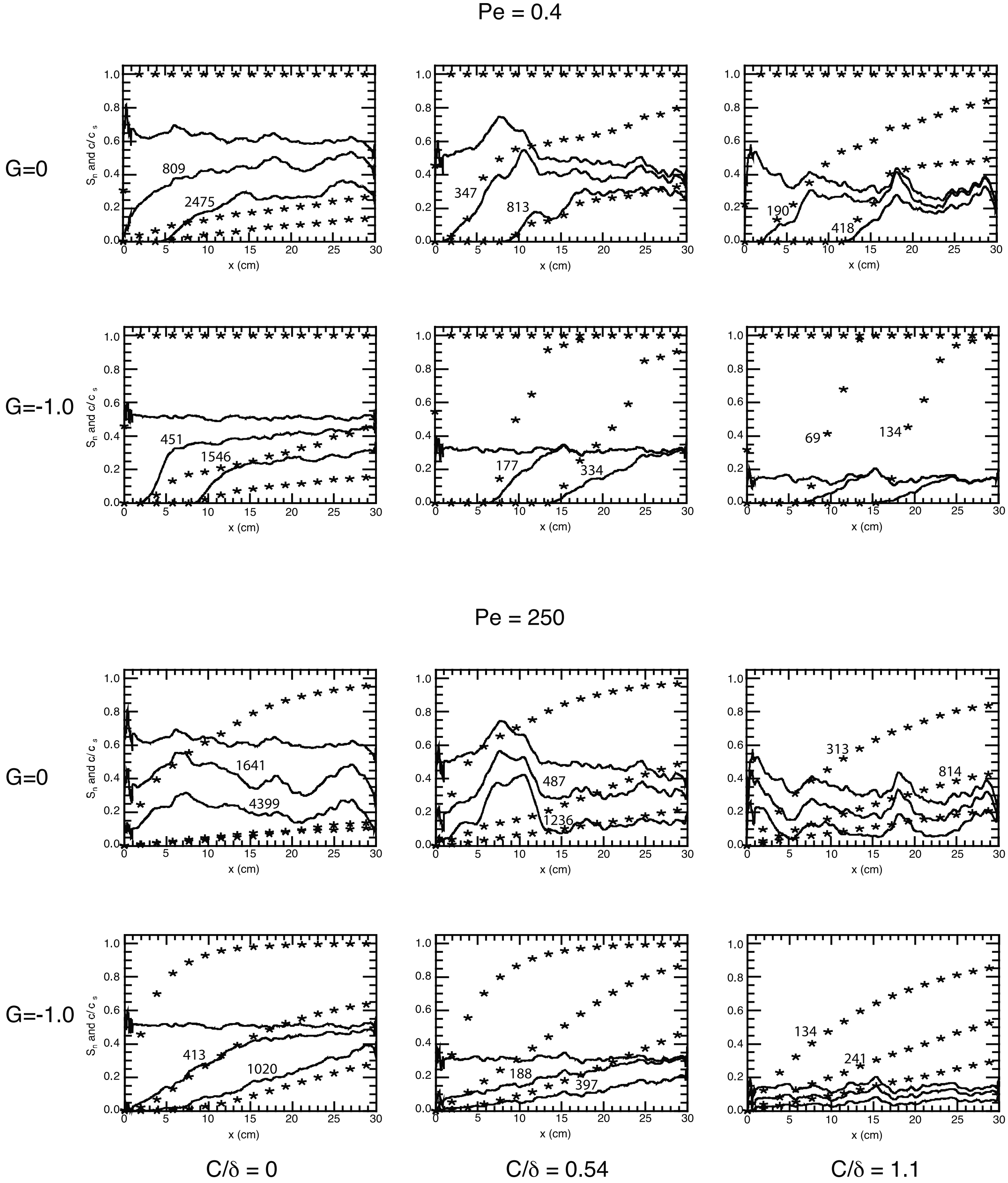

Figure 5. Saturation (lines) and normalized concentration (points) profiles for simulations (flow is from left to right) with initial conditions shown in Figure 2. The three profiles represent the conditions in the fracture at $S_n = S_{no}$, $1/3S_{no}$, and $2/3S_{no}$. For each plot, the largest values of S_n and c coincide with the initial condition and both values decrease monotonically with time. The numbers adjacent to the $S_n = 1/3S_{no}$ and $2/3S_{no}$ curves reflect the cumulative number of pore volumes flowed through the fracture at the time the profiles were recorded.

by integrating across the width of the fracture ($S_n(x)$ and $c(x)$) at different times to understand the progression of dissolution and mass removal with time. $S_n(x)$ is calculated using a $128\Delta x \times L_y$ averaging window on the binarized saturation field, and $c(x)/c_{eq}$ is the flux-weighted concentration at each cross section along the flow direction normalized by the equilibrium concentration of the dissolved nonaqueous phase. Figure 5 shows $S_n(x)$ (solid lines)

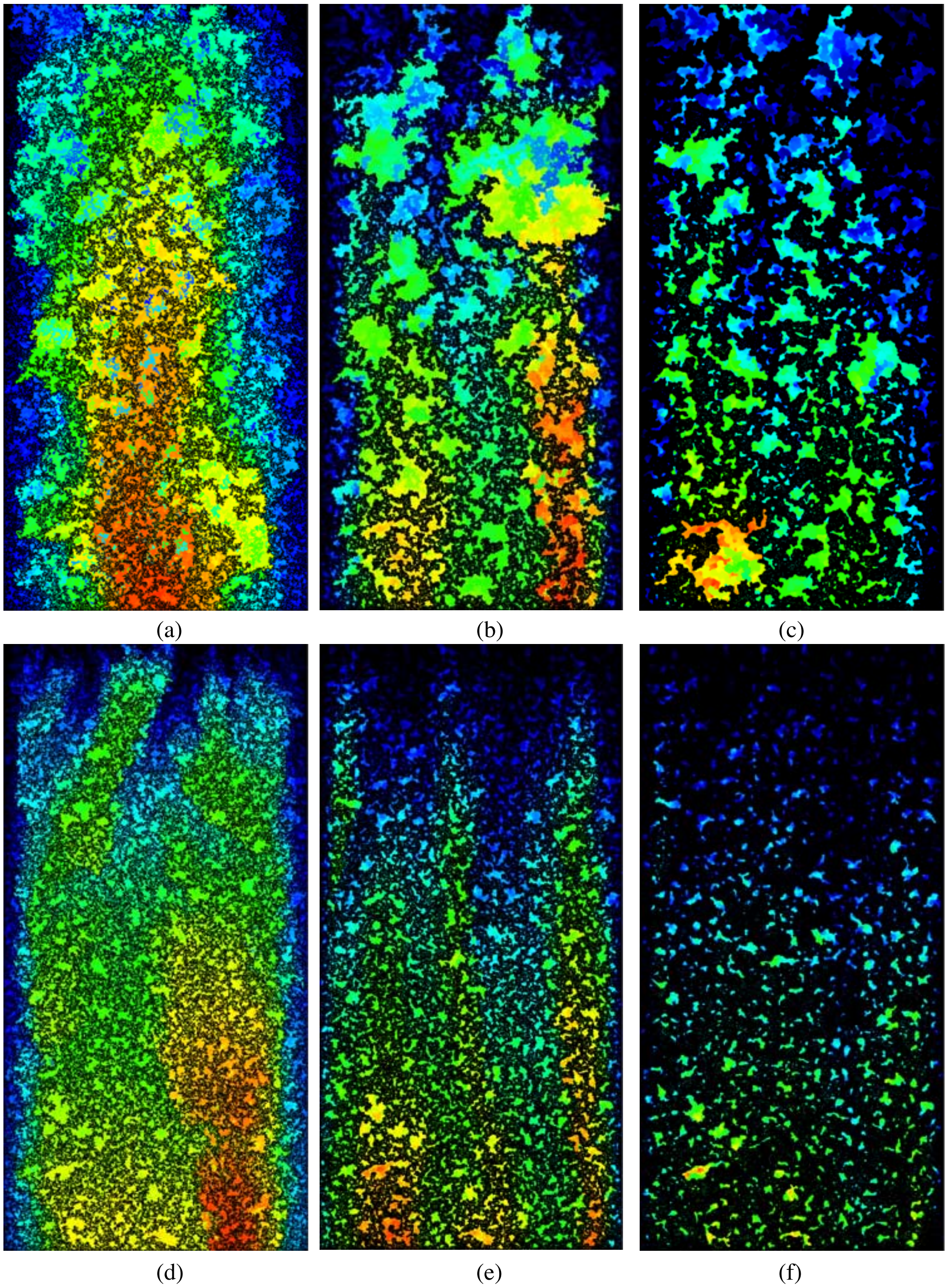

Figure 6. Composite images of entrapped phase evolution during dissolution simulations with flow from top to bottom. The values of C/δ and G correspond to the initial entrapped phase distributions shown in Figure 2. The color scale (blue-green-yellow-red) represents the order in which cells originally filled with the entrapped phase were replaced by water owing to mass transfer (blue first; red last), and black represents locations that were initially water-saturated.

and $c(x)$ (symbols) plotted against the distance into the fracture, x, for the initial phase distributions represented in Figure 2. The different curves for each plot represent profiles calculated from the simulations, at $S_n = S_{no}$, 2/3 S_{no} and 1/3 S_{no}. The profiles are shown for $Pe_0 = 0.4$ and 250. These plots demonstrate the wide range of behaviors exhibited by the simulations. In the discussions in this section, we focus on saturation and concentration profiles and the spatial patterns of dissolution, using S_n as a surrogate variable to describe time evolution. In reality, the time scales over which the changes in S_n occur vary widely between the different cases, and we will address these differences in section 4.2.3.

[28] At high Pe_o, dissolution occurs relatively uniformly over the length of the fracture, particularly for low C/δ and $G = 0$. This type of behavior occurs because at high Pe_o (250), water flows through the fracture rapidly, before picking up enough dissolved nonaqueous phase to reach the equilibrium concentration. As discussed below, this type of behavior is also in part due to the formation of dissolu-

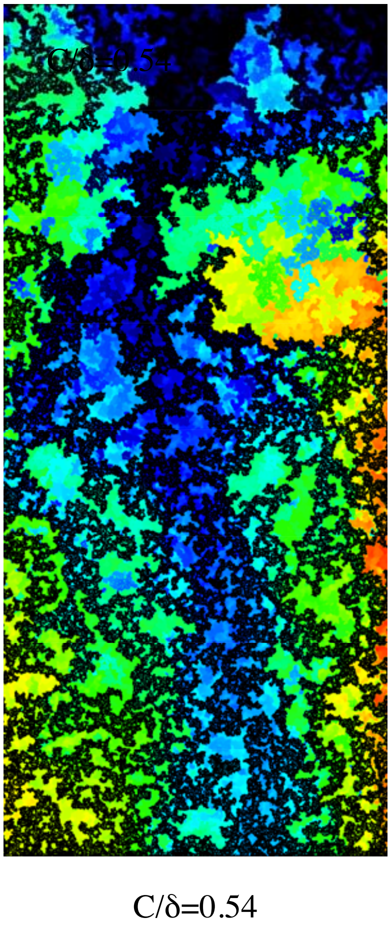

Figure 7. Composite image of entrapped phase evolution for the initial conditions shown in Figure 1b, with 100 grid block strips removed from each of the long edges. The resulting dissolution pattern is similar to that shown in Figure 5 (entire field) except that the early channel forms through the middle of the domain instead of along the edges. This suggests that the initial low saturations along the fracture edges resulting from the invasion simulations do not introduce any artifacts in the behavior of mass transfer rates.

tion fingers. Focused flow through dissolution fingers sustains low concentrations of the dissolved nonaqueous phase farther into the fracture. As a result, the width-averaged dissolution rate is relatively uniform along the fracture length and the width-averaged saturation $S_n(x)$ decreases relatively uniformly along the entire fracture length. At lower values of $Pe_o(0.4)$, the formation of a distinct dissolution front is evident as $S_n(x)$ decreases to zero over a length that extends from the entrance to the front location (which advances into the fracture with time). Note that for the $C/\delta = 0$ cases at $Pe_0 = 0.4$, the formation of a dissolution front is also accompanied by dissolution along the length of the fracture downstream of the front (The $S_n(x)$ profiles reveal a progressive decrease from $S_{no}(x)$ values downstream of the front location for $C/\delta = 0$, and to a lesser extent for $C/\delta = 0.54$ and 1.1 with $G = 0$). To clarify the cause of the different behaviors observed in Figure 5, Figure 6 shows composite images of the dissolution process for the initial conditions shown in Figure 2. These images show the order in which locations initially filled with nonaqueous phase are replaced by water as interphase mass transfer reduces the volume of each of the entrapped regions. The simulations depicted in Figure 6 were each run with $Pe_o = 10$, which falls between the two different cases shown in Figure 5.

[29] For the $C/\delta = 0$, $G = 0$ simulation (Figure 6a), the initial invading phase structure lacks a multitude of connected paths traversing the length of the fracture, due to the contorted shapes of the large entrapped areas that span a significant fraction of the fracture width. Connected paths are available along the lateral edges of the domain and dissolution fingers form quickly along these edges. Mass transfer occurs predominantly by transverse diffusion from the outer edges of the entrapped regions (inner edges of the fingers). As the entrapped phase dissolves gradually from these regions, the fingers widen laterally. At the same time, there is a readjustment of the shapes of entrapped regions by capillary forces: although mass transfer occurs predominantly along the outer edges, the way that a single entrapped region responds to mass removal incorporates the influence of capillary forces. Interface retraction does not always occur from the regions of highest mass transfer. Thus, there is a gradual redistribution and breakup of the nonaqueous phase within the central region, leading to increased flow through this region. This is observed as the isolated regions of cool colors in the interior of the low-flow region in Figure 6a, which correspond to nonaqueous phase that vacated these locations at early times. Overall, the initial formation of fingers along the edges and diffusion-controlled mass transfer from the periphery of the central region are the dominant controls in this case, leading to relatively uniform width-integrated dissolution along the fracture length, observed in the saturation profiles (Figure 5, $C/\delta = 0$, $G = 0$, $Pe_o = 250$). At lower $Pe_o \sim 0.4$, the relative influence of diffusion is stronger. Transverse diffusion from the inner edges of the entrapped regions bordering the fingers is still the dominant mechanism for mass transfer in the downstream regions of the fracture. Also, near the fracture entrance, because of relatively slow advection, diffusion controls mass transfer along the upstream edge of the entrapped region. Thus, the flowing phase reaches equilibrium shortly after encountering regions of entrapped phase leading to the formation of a dissolution front. Thus, at lower Pe_o, in the $C/\delta = 0$, $G = 0$ case, a mixed dissolution front/uniform dissolution behavior results (Figure 5, $C/\delta = 0$, $G = 0$, $Pe_o = 0.4$).

[30] For $C/\delta = 0.54$ and $G = 0$ (Figure 6b), the entrapped regions are more compact and do not span a large fraction of the fracture width as in the $C/\delta = 0$, $G = 0$ case. Thus, the mobile phase penetrates and flows through the central portion of the fracture width even at early time, leading to the formation of dissolution fingers along the edges and the center of the fracture. However, the overall behavior of the width-averaged saturation profiles is not significantly different from that observed in the $C/\delta = 0$, $G = 0$ cases. The dominant mechanism of mass transfer involves transverse diffusion at the edges of the dissolution fingers, especially in the downstream portions of the fracture. Thus, at high Pe_o (Figure 5, $C/\delta = 0.54$, $G = 0$, $Pe_o = 250$), there is relatively uniform width-integrated dissolution along the length of the

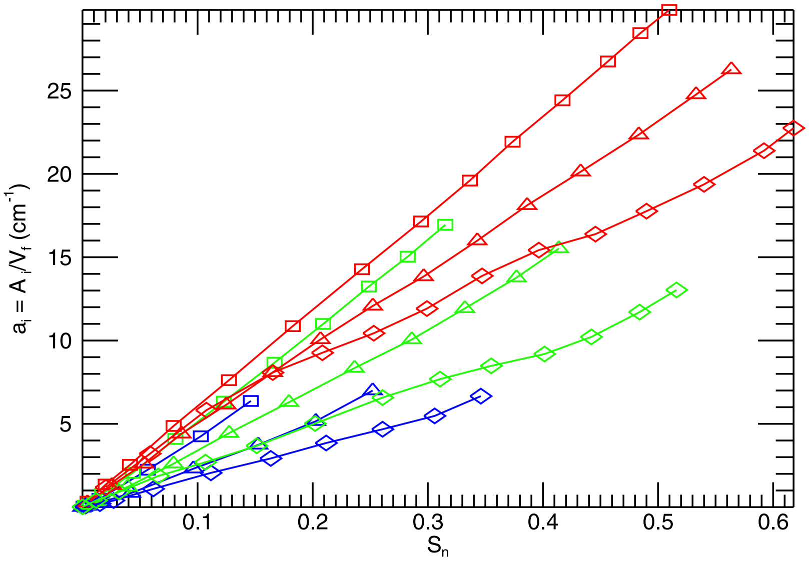

Figure 8. Specific interfacial area (a_i) plotted against entrapped phase saturation (S_n) for $G = 0$ (diamonds), -0.25 (triangles), and -1.0 (squares) and $C/\delta = 0$ (red), 0.5 (green), and 1 (blue). The nearly linear relationship between a_i and S_n supports the use of a simple constitutive relationship (equation (15)).

fracture and at low Pe_o, (Figure 5, $C/\delta = 0.54$, $G = 0$, $Pe_o = 0.4$), a mixed dissolution front/uniform dissolution behavior results. Note that the channels along the lateral edges of the fracture for the $C/\delta = 0$ and 0.54, $G = 0$ simulations are a result of the initial configuration of the nonaqueous phase, which includes narrow strips of low saturation/high transmissivity along the edges of the fracture. This is a result of the open boundaries used during the invasion simulations, which causes the wetting invading phase to completely displace the nonwetting defending phase along the boundaries. Removing the initial channels along the edges by clipping the domain (e.g., for $C/\delta = 0.54$ and $G = 0$ case), leads to the formation of a single dominant channel through the middle of the fracture separating two low-flow regions along either side of the domain (Figure 7). These two separate regions are quite similar to the single low-flow region shown in the corresponding full field simulation (Figure 6b), in the sense that transverse diffusion from the edges of the dissolution fingers is the dominant mass transfer mechanism in these cases, regardless of the boundary effects involved in the invasion simulations.

[31] The main difference between the $C/\delta = 1.1$, $G = 0$ and the other $G = 0$ cases is that the entrapped regions are much smaller and more compact, and there are larger open areas between them for the invading fluid to flow through. As a result, a larger number of dissolution fingers/channels are formed (Figure 6c). There is more mass transfer all along the periphery of individual entrapped regions, because they are in contact with more than one dissolution finger/channel. The overall behavior of the $S_n(x)$ profiles for this case is still strongly controlled by Pe_o. The relatively lower diffusive fluxes in the high Pe_o case leads to relatively uniform dissolution along the fracture length throughout the duration of the simulation, while a mixed dissolution front/uniform dissolution behavior is seen at low Pe_o.

[32] In the $G = -1.0$ cases, the individual entrapped regions are substantially smaller than in the corresponding $G = 0$ cases (Figure 2). However, the spatial distribution of the entrapped regions is strongly affected by C/δ. For $C/\delta = 0$ (Figure 2d), the entrapped regions are closely spaced, reducing the relative permeability to the invading phase significantly, while in the $C/\delta = 0.54$ and 1.1 cases, the spacing progressively increases. There is still a tendency for dissolution fingers to form, owing to spatial variations in entrapped phase saturation, rather than occlusion by large individual entrapped regions. Qualitatively, the behavior in the $G = -1.0$ cases (Figures 6d–6f) follow similar trends to the $G = 0.0$ cases (Figures 6a–6c), except that the small sizes of the entrapped regions lead to the formation of more dissolution fingers and these fingers are much wider than in the $G = 0.0$ cases. The $S_n(x)$ profiles shown in Figure 5 also suggest a qualitative similarity between the $G = 0.0$ and $G = -1.0$ cases at low $Pe_o = 0.4$, in that a dissolution front forms in both sets of simulations. At high $Pe_o = 250$, there are greater differences between the behavior for the $G = -1.0$ and $G = 0.0$ cases. At $C/\delta = 0$ and 0.54, a mixed dissolution front/uniform dissolution behavior is observed in the $G = -1.0$ cases, unlike the uniform dissolution in the $G = 0.0$ cases. This is largely because in the $G = -1.0$ case, the small entrapped regions are more readily dissolved away and there are more fingers.

4.2.2. Intrinsic Interfacial Area and Relative Permeability

[33] The intrinsic interfacial area (a_i) plays a critical role in fracture-scale mass transfer rates. Here we quantify the evolution of a_i as the nonaqueous phase dissolves. Figure 8 shows a_i plotted against S_n for $C/\delta = 0.5$, 1, 2; $G = 0$, -0.25, -1.0; and $Pe_o = 10$. For all simulations, as mass transfer causes S_n to decrease from S_{no}, a_i decreases approximately linearly from the values of a_{io} modeled by (14) to zero at $S_n = 0$. This behavior is consistent across

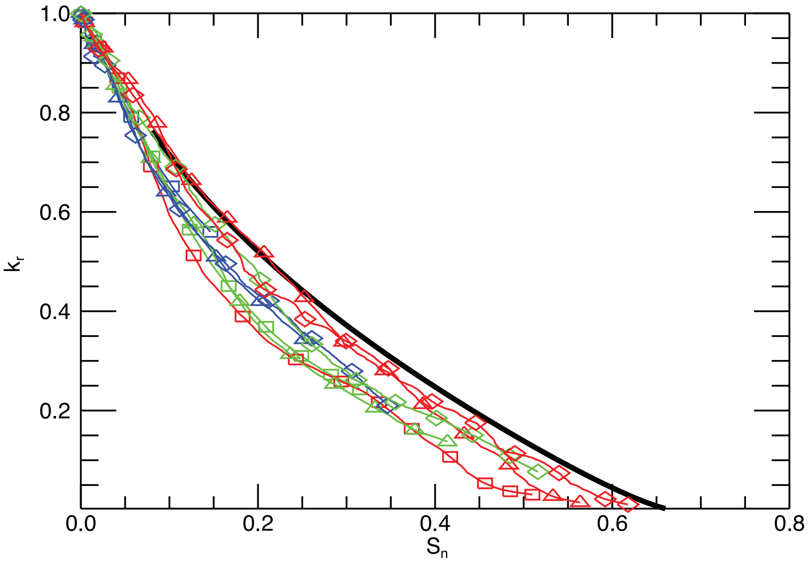

Figure 9. Relative permeability (k_r) plotted against entrapped phase saturation (S_n) for G = 0 (diamonds), −0.25 (triangles), and −1.0 (squares) and C/δ = 0 (red), 0.54 (green), and 1.1 (blue). The black line represents k_{rs} calculated using the parameters from *Detwiler et al.* [2005], which were determined from high-resolution mechanistic simulations in similar aperture fields.

the range of Pe_o (not shown) and is consistent with similar observations in measurements of interfacial area in porous media [e.g., *Johns and Gladden*, 1999; *Schnaar and Brusseau*, 2005; *Zhang et al.*, 2002]. This suggests that the evolution of a_i can be represented well using a relationship of the form

$$a_i = a_{io}\frac{S_n}{S_{no}} \tag{15}$$

such that the dependence of a_i on C/δ and G is introduced by a_{io}, which can be estimated using equation (14).

[34] The relative permeability (k_r) of the fracture changes as the entrapped nonaqueous phase dissolves. Relative permeability plotted against S_n for all of the simulations (Figure 9) demonstrates that k_r shows a similar dependence on S_n despite the fact that the entrapped phase morphology varies widely between simulations and over the duration of individual simulations. In a previous study [*Detwiler et al.*, 2005], we proposed a semiempirical relationship for the satiated relative permeability (i.e., corresponding to the initial entrapped phase distribution) of variable aperture fractures over the same range of C/δ with the form

$$k_{rs} = \frac{\langle b_n\rangle^3}{\langle b\rangle^3}\left[\left(1-\frac{S_n}{S_n^*}\right)\left(1+\frac{S_n}{S_n^*}\right)\bigg/\left(1+\frac{S_n}{t'(S_{nI})}\right)\right]^{t'} \tag{16}$$

where, $\langle b_n\rangle$ is the mean aperture occupied by the entrapped phase, S_n^* is the percolation threshold, S_{nI} is a constant that determines the slope of the k_{rs} versus S_n curve as $S_n \to 0$, and t' is the conductivity exponent for two-dimensional percolation systems (∼1.3). Though k_{rs} is a measure of k_r when the entrapped regions are distributed more or less uniformly over the fracture area (a condition that is not satisfied as dissolution progresses from the initial entrapped phase), we expect k_{rs} to provide reasonable estimates of k_r. When dissolution leads to nonuniform spatial distributions of entrapped regions, the corresponding fracture-scale values of k_r will be overestimated by (16). Despite this limitation, Figure 9 demonstrates that the k_{rs} model provides a reasonable upper bound for k_r from all of the simulations. Furthermore, it is reasonable to expect that applying (16) as an estimate of local relative permeabilities within subregions of the fracture would improve agreement between model and simulations, because the influence of channels parallel to the flow direction would be better represented in the modeled results (see section 5).

4.2.3. Interphase Mass Transfer Rates

[35] As discussed in the introduction, mass transfer rate coefficients are often derived from experimental results by applying the solution to the one-dimensional advection-reaction equation (1) to either measured outflow concentrations, or, if available, concentration profiles within the experiment. Applying these rate coefficients in different fractures or at different scales requires that the distribution of entrapped phase is similar. Despite the complex initial entrapped phase distributions, for all cases the entrapped phase is distributed relatively uniformly throughout the fracture. However, as dissolution progresses dissolution fronts and/or dissolution fingers begin to form undermining our ability to apply mass transfer rate coefficients at the fracture scale. Figure 10 shows examples of fitting (2), with $C(x)$ in place of C and x in place of L, to concentration profiles at t = 0 for C/δ = 0, G = 0 and C/δ = 1.1, G = −1 at Pe_o = 0.4, 10 and 250. The fitted curves demonstrate that the one-dimensional advection-reaction model fits the initial width-averaged concentration profiles quite well over a wide range of Pe_o, suggesting that this approach provides reasonable estimates of k (and Sh) when the entrapped phase is relatively uniformly distributed.

[36] Estimates of k were obtained by fitting (2) to concentration profiles from each of the simulations at t = 0. By plotting $Sh = k\,\langle b\rangle/D_m$ versus Pe_o for different initial

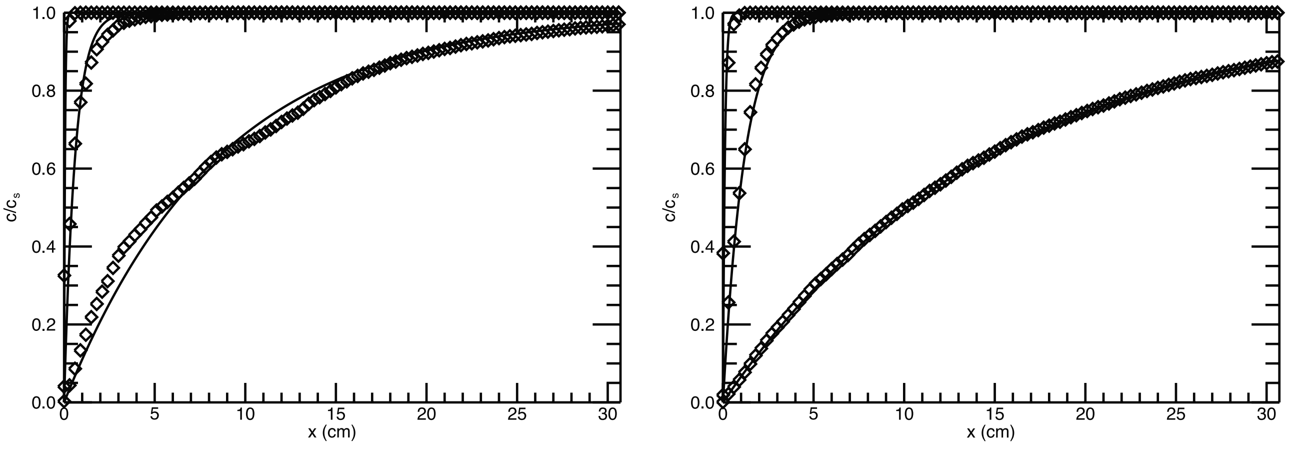

(a) (b)

Figure 10. Initial concentration profiles (diamonds) for (a) $G = 0$, $C/\delta = 0$ and (b) $G = -1$, $C/\delta = 1.1$ with results from fitting a one-dimensional advection-reaction equation (lines) to the profiles for $Pe = 0.4$, 10, and 250.

entrapped phase distributions (not shown) we inferred a simple relationship for *Sh*:

$$Sh = n_1 Pe_o^{n_2} \tag{17}$$

where n_1 and n_2 are fitted parameters. Fitting (17) to the complete data set provides estimates of n_1 and n_2 of 0.7 and 0.23. Figure 11 shows $Sh/Pe_o^{0.23}$ plotted against S_{no}. Despite the wide variation in the morphologies of the entrapped phase structures, *Sh* was found to be approximately constant for much of the range of S_{no}, particularly at larger Pe_o. For all values of Pe_o, *Sh* was found to decrease near the percolation threshold and for smaller values of Pe_o, *Sh* decreased as S_{no} approached zero. However, the variations in *Sh* with S_{no} were similar in magnitude to the interrealization variability exhibited for the $G = 0$ simulations, suggesting the absence of a systematic dependence on S_{n0}. This supports the use of (17) to approximate *Sh*. The influence of S_{no} on mass transfer rates is reflected predominantly through the relationship for a_{io} given by (15). Extending the same idea further, we expect that *Sh* from (17) could be used together with a_i given by (15) to describe mass transfer as the entrapped phase geometry evolves during dissolution. In section 5, we demonstrate the accuracy of this representation.

5. Applying Constitutive Relationships to a Continuum Model

[37] Results in section 4 suggest that over a range of parameter space, fracture-scale interphase mass transfer may

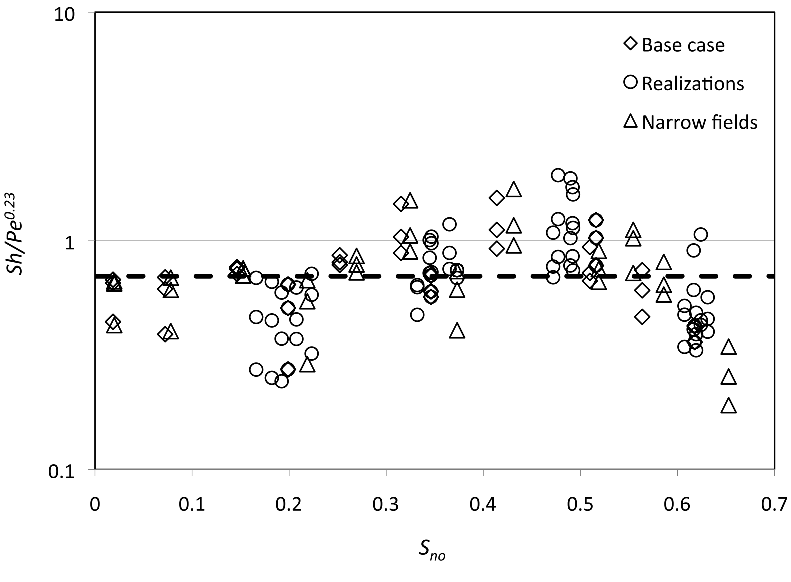

Figure 11. Sherwood number (*Sh*) normalized by $Pe_o^{0.23}$ plotted against S_{no} for all simulations. The results include the base case simulations ($C/\delta = 0$, 0.54, 1.1, 2.2; $G = 0.0$, -0.5, -1.0; $Pe_o = 0.4$, 10, 250) and simulations in the corresponding narrow fields (i.e., 100 grid block strip removed from each long edge of the fracture) and multiple realizations for the $C/\delta = 0$ simulations.

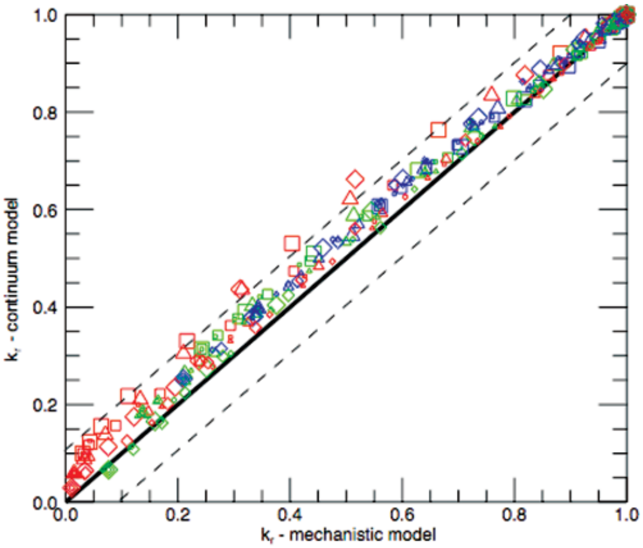

Figure 12. The relative permeability, k_r from continuum model simulations using the constitutive relationships in (15), (16), and (17) plotted against k_r measured during the mechanistic simulations for $G = 0$ (diamonds), -0.25 (triangles), -1.0 (squares); $C/\delta = 0$ (red), 0.54 (green), 1.1(blue), 2.2 (magenta); and $Pe_o = 0.4$ (small), 10 (medium), 250 (large). The dashed lines represent a ± 10% discrepancy between estimates of k_r calculated using the continuum model and mechanistic model.

be represented by a set of relatively simple constitutive relationships for a_i, k_r, and Sh. The relationships for k_r and Sh describe steady state mass transfer for the initial (satiated) entrapped phase distribution quite well. However, in many of the simulations, transient dissolution led to nonuniform evolution of the entrapped phase (Figure 6) suggesting that these fracture-scale relationships will be less effective at quantifying evolving mass transfer rates at later times. Thus, rather than applying these constitutive relationships to the entire fracture, we coarsen the grid used in the mechanistic simulations and apply the constitutive relationships locally. This approach provides a continuum model of mass transfer and dissolution that does not require explicit discretization of each entrapped region, but instead relies upon locally averaged estimates of $\langle b \rangle$ and S_n. Using a continuum representation of the variable aperture fracture, where the grid dimensions are large enough that S_n is well behaved (i.e., maximum $S_n \sim S_{no}$) and small enough that intermediate-scale features such as dissolution fingers and fronts can be represented, may provide an effective approach for representing dissolution from variable aperture fractures and fracture networks at a much wider range of scales than is feasible with the detailed mechanistic model.

[38] Numerical implementation of a local mass transfer model using the relationships for a_i, k_r and Sh in (15), (16) and (17) provides estimates of mass transfer from the fracture over the range of parameter space. To implement this model, we coarsened the initial aperture field and saturation fields such that each grid block contained an average over a 128 × 128 region (1.92 × 1.92 cm) of the initial fine grid. The coarse grid hydraulic apertures (b_h) are calculated as the geometric mean of the fine grid values and the saturations are the average of the binary saturation field at the end of the invasion simulation. The result is an 8 × 16 domain that represents the original 1024 × 2048 fracture. Local transmissivities incorporate values of k_r calculated from the local value of S_n and equation (16), and allow for the solution of the pressure field and local flow rates using a two-dimensional flow solver

$$\nabla \cdot (T \nabla h) = 0 \tag{18}$$

where

$$T = k_r \frac{b_h^3 g}{12\nu} \tag{19}$$

Mass transfer and transport of the dissolved nonaqueous phase are calculated using a two-dimensional advection-dispersion-reaction equation of the form

$$\nabla \cdot \left(\mathbf{V}\bar{b}\bar{c}\right) - \nabla \cdot \left(\mathbf{D}\bar{b} \cdot \nabla\bar{c}\right) = ShD_m a_i \left(c_{eq} - \bar{c}\right) \tag{20}$$

where the mean velocity vector, $\mathbf{V}$, is given by

$$\mathbf{V} = T\nabla h \left[\frac{1}{\bar{b}\Delta x(1 - S_n)}\right] \tag{21}$$

where $\bar{b}$ is the effective transport aperture (the arithmetic mean of the initial aperture field), $\bar{c}$ is the averaged concentration, and $\mathbf{D}$ is a dispersion tensor. We approximate $\mathbf{D}$ using a relationship presented by *Detwiler et al.* [2001] for dispersion in saturated fractures:

$$\frac{\mathbf{D}}{D_m} = 1 + \alpha_{macro} Pe + \alpha_{Taylor} Pe^2 \tag{22}$$

where α_{macro} and α_{Taylor} are the dispersion coefficients associated with in-plane and out-of-plane velocity variations and have values of 2.0 and 1/210, respectively, for the fractures used in our study. Though (22) likely underestimates dispersion in partially saturated fractures [e.g., *Detwiler et al.*, 2002], we expect dissolution simulations to be relatively insensitive to estimates of the dispersion tensor, as discussed by *Detwiler et al.* [2001]. Interphase mass transfer leads to reductions in nonaqueous phase saturations that are calculated using

$$\rho_n \bar{b} \frac{\partial S_n}{\partial t} = ShD_m a_i \left(c_{eq} - \bar{c}\right) \tag{23}$$

To investigate the ability of the continuum model to predict interphase mass transfer under a range of conditions, we applied the model to the evolving saturation fields calculated during the mechanistic simulations. This resulted in steady state estimates of k_r and J at each time step that can be directly compared to the corresponding values calculated during the mechanistic simulations. Figure 12 shows k_r calculated using the coarse grid flow model (19) and k_r calculated during each time step of the mechanistic simulations. The results show that applying (16) locally yields good agreement between the two models. The continuum model systematically overestimates k_r by less than 10% for most of the cases, which is considerably better

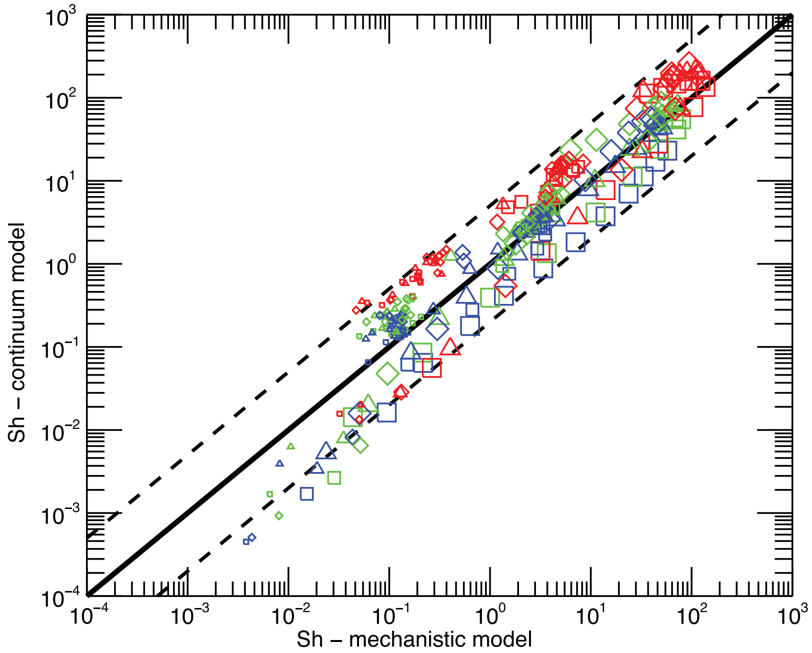

Figure 13. *Sh* predicted by the continuum model simulations using the constitutive relationships in (15), (16), and (17) plotted against *Sh* measured during the mechanistic simulations for $G = 0$ (diamonds), -0.25 (triangles), -1.0 (squares); $C/\delta = 0$ (red), 0.54 (green), 1.1(blue), 2.2 (magenta); and Pe_o = 0.4 (small), 10 (medium), 250 (large). The data points represent mass transfer rates over the entire duration (full range of S_n) of each simulation. The dashed lines represent discrepancies of factors of 1/5 and 5 between the continuum model calculations and the mechanistic model calculations.

than the results shown in Figure 9 where (16) was applied at the scale of the entire fracture. At large Pe_o and $C/\delta = 0$, discrepancies are slightly larger, because (16) predicts small but significant values of k_r in the central region of the fracture; however, owing to very limited connection of the flowing phase in this region, the mechanistic model predicts very little flow through this region.

[39] We use (20) with local values of *Sh* estimated using (17) to predict fracture-scale mass transfer rates observed in the mechanistic simulations over the full range of S_n. Figure 13 compares evolving values of fracture-scale *Sh* for the two different models. As expected from the variability observed in Figure 11, there are more significant discrepancies between estimates of *Sh* than we observed for k_r. However, almost all of the coarse grid estimates fall within half an order of magnitude (dashed lines) of the values predicted by the mechanistic model. These discrepancies are predominantly due to the relatively wide variability in the values of *Sh* measured from the mechanistic simulations. Though the constitutive model does not represent the interrealization variability in *Sh*, (Figure 13), the absence of significant systematic trends away from the mechanistic model results over the full range of S_n is encouraging.

[40] Equations (18)–(20) also allow transient simulations of dissolution by using the initial entrapped phase distribution for calculating coarse grid values of S_{no} and evolving S_n according to (23). Figure 14 compares the width-integrated saturation profiles presented in Figure 5 to profiles calculated using the transient numerical implementation of equations (18)–(23). Each of the profiles are shown at $S_n = S_{no}$, $2/3S_{no}$, and $1/3S_{no}$ and thus reflect the spatial variability of dissolution within the fracture, but not the time variation of the dissolution rates. The continuum model cannot be expected to predict the small-scale variability observed in the mechanistic simulations, but the large-scale trends are reproduced quite well (Figure 14). The poorest agreement occurs for the $G = 0$, $C/\delta = 0.54$, $Pe_o = 0.4$ simulation, where the large entrapped regions observed in the range $5 < x < 12$ cm dissolve considerably more slowly during the continuum simulations. This is because there are several coarse grid blocks in this region where $S_{no} = 1.0$ and thus the predicted mass transfer rate at early times is zero. By contrast, the mechanistic model allows capillarity to break up these large entrapped regions at relatively early times (see blue regions in Figure 6b), leading to enhanced mass transfer and faster dissolution rates.

[41] To compare fracture-scale dissolution rates between the continuum and mechanistic models, we use the total number of pore volumes required for complete dissolution as a metric. This is a stringent metric because the errors in the mass transfer rate (Figure 13) tend to have the same sign (i.e., errors accumulate) throughout the duration of a simulation. Figure 15 shows the total number of pore volumes required for complete dissolution of the entrapped phase using the mechanistic model and the continuum model with the constitutive relationships developed in section 4. The total number of pore volumes required for dissolution across these initial phase structures and flow conditions covers a range of 2.5 orders of magnitude. Over this entire range, the continuum model predicts the total pore volumes required for dissolution to within a factor of two (dashed lines) for most of the parameter values. The exceptions are at $G = 0$, $C/\delta = 0.54$ and 2.2, where the continuum model overestimates the pore volumes required for dissolution and at

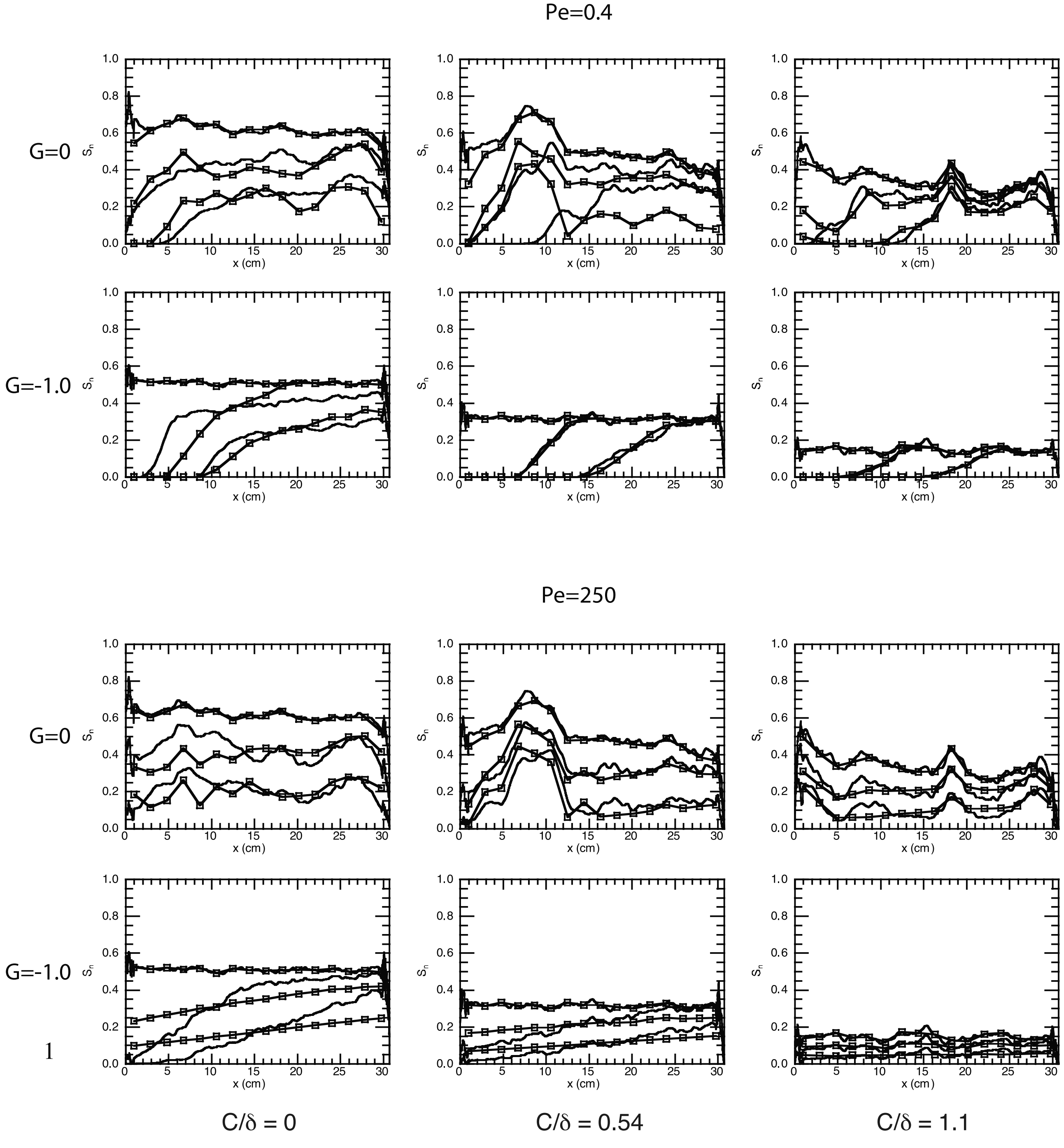

Figure 14. Saturation profiles for the mechanistic simulations on a 1024 × 2048 grid (lines) and the continuum model simulations on a coarsened 8 × 16 grid using the constitutive relationships developed in section 4 (lines with squares). The profiles correspond to the results shown in Figure 5, and the three profiles represent the conditions in the fracture at $S_n = S_{no}$, $1/3S_{no}$, and $2/3S_{no}$.

$C/\delta = 0$, $G = -0.25$ and -1.0, where the continuum model underestimates the pore volumes required for dissolution. For the $G = 0$ cases, the discrepancy reflects the influence of the relatively slow dissolution of the large entrapped region in the range $5 < x < 12$ cm during the continuum model simulations as observed in Figure 14. For the $G = -0.25$, -1.0 and $C/\delta = 0$ cases, the relatively uniform distribution of smaller entrapped regions results in a near uniform S_{no} field for the continuum simulations. Thus, continuum model simulations predict a relatively uniform dissolution front propagating through the fracture, whereas the mechanistic simulations are influenced by small-scale heterogeneity in S_{no} that result in a nonuniform (and slower) dissolution process (Figure 6d). However, despite small variations in predicted rates and spatial evolution of the entrapped phase, the ability of the continuum model to predict the transient dissolution patterns over a broad range of parameter space demonstrates that a relatively simple set of constitutive relationships based solely upon S_n are adequate for predicting the evolution of entrapped phase saturations in a

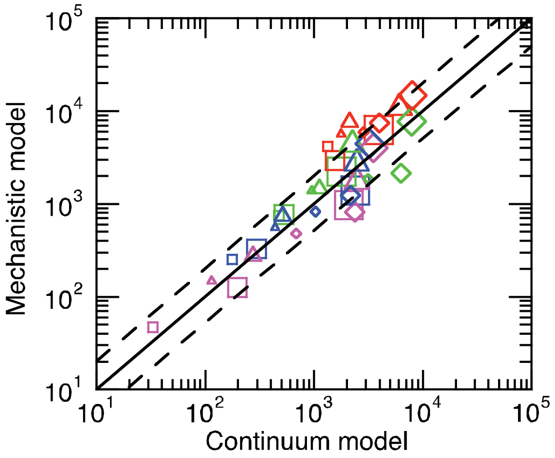

Figure 15. Pore volumes required for complete dissolution estimated by the continuum model simulations plotted against the same results for the mechanistic simulations for $G = 0$ (diamonds), -0.25 (triangles), -1.0 (squares); $C/\delta = 0$ (red), 0.54 (green), 1.1(blue), 2.2 (magenta); and $Pe_o = 0.4$ (small), 10 (medium), 250 (large). The dashed lines each represent a factor of 2 deviation from the mechanistic simulations.

variable aperture fracture. The most surprising feature of these results is that a zeroth-order measure of entrapped phase distribution (S_n) is sufficient for predicting mass transfer from the complex and varied entrapped phase structures observed in Figure 2.

6. Concluding Remarks

[42] We have demonstrated the influence of entrapped phase structure on interphase mass transfer and dissolution in variable aperture fractures over a range of the dimensionless parameters C/δ, G, and Pe_o, which reflects a wide range of aperture field geometries, invasion processes and flow rates, respectively. A series of high-resolution mechanistic simulations based on the rigorously tested approach of *Detwiler et al.* [2001] demonstrated the detailed interactions between fluid flow, dissolved phase transport, capillary forces and evolution of entrapped phase geometry. These simulations provided a detailed picture of spatial and temporal variations in mass transfer rates in fractures with initial entrapped phase saturations that ranged from zero to near the percolation threshold, and included widely varying entrapped phase geometries. The high-resolution mechanistic simulations also provided a "ground truth" against which to evaluate simplified constitutive models of the coupled processes that can be incorporated in continuum models. A significant focus of this paper was on the development of such constitutive relationships based on the results of the high-resolution simulations. Somewhat surprisingly, the results demonstrated that across a wide range of initial entrapped phase geometries and flow rates, a zeroth-order measure of entrapped phase structure, the entrapped phase saturation (S_n), serves as a reasonably sufficient controlling parameter in constitutive relationships for quantifying local estimates of relative permeability and intrinsic interfacial area. In addition, when combined with a simple power law relationship for the Sherwood number as a function of Peclet number, these constitutive relationships provide estimates of local interphase mass transfer rates. Coarse grid continuum simulations using these simplified constitutive relationships compared reasonably well with the high-resolution mechanistic simulations, both in terms of the time to total dissolution and the spatial evolution of the entrapped phase saturation during dissolution. The number of pore volumes required for complete dissolution was predicted by the coarse grid simulations to within a factor of two for almost all cases. The coarse grid simulations also consistently predicted differences in overall behavior of the width-integrated dissolution process, in terms of when a dissolution front forms and when there is a relatively uniform dissolution rate across the fracture length.

[43] Discrepancies between the high-resolution simulations and coarse grid simulations based upon the proposed constitutive relationships were the largest for $G = 0$ and small values of C/δ. This reflects fractures in which the influence of in-plane curvature is negligible and the interface geometry can be predicted by standard invasion percolation. In these fractures, the entrapped phase occupies tortuous clusters that span a broad range of length scales. Dissolution of these clusters can result in nonlocal changes in saturation due to the subtle disconnection between local mass transfer rates and the resulting interface movement. As noted in section 4.2.1 (see also Figures 6a and 6b), the overall evolution of blob shape is strongly influenced by capillary forces because the blobs do not necessarily recede away from regions of high mass transfer. Clearly the constitutive relationships used in the continuum model are incapable of accurately replicating the influence of these subtle processes, especially the role of capillary forces, in controlling blob shape evolution. However, despite this implicit simplification in the continuum model, when continuum simulations do not include large regions of the coarse grid in which S_n is greater than the percolation threshold and $k_r = 0$, this limitation results in negligible discrepancies. Furthermore, these limitations arise in small C/δ fractures which involve a combination of very small mean aperture relative to correlation length and aperture variability and/or weakly wetting fluids; measurements of natural fracture surfaces [e.g., *Brown*, 1995] suggest that C/δ in natural fractures (assuming perfect wettability of one of the fluids) is typically greater than 0.5.

[44] Our parametric studies focused entirely on initial entrapped phase structures that resulted from either capillary displacements ($G = 0$) or gradient stabilized displacements (negative G). There are also problems of interest in which a phase becomes entrapped as the result of an unstable displacement, such as when a DNAPL migrates through steeply dipping fractures [e.g., *Ji et al.*, 2004; *Nicholl and Glass*, 2005]. This can result in the formation of fingers along the displacement front and a much less uniform distribution of the phases than was observed in our simulations. Our proposed constitutive relationships are not appropriate for predicting mass transfer from the entrapped phase in this situation owing to the large contiguous regions ($S_n = 1$) of entrapped phase. However, as in the case of DNAPL dissolution, often we are interested in mass transfer from the invading phase after the source is removed and the initial invading phase becomes entrapped by capillary

forces. In this case, our continuum model should predict flow and mass transfer reasonably well if the scale of the simulation grid is finer than the scale of the fingers that formed during the initial displacement. Furthermore, it is likely that a significant portion of the DNAPL will drain from the initial fingers and will become entrapped in subhorizontal fractures, leading to entrapped phase structures within these fractures that are quite similar to those investigated in this paper (e.g., see Figure 2).

[45] Finally, our models neglect the influence of interactions with a potentially porous/permeable matrix bounding the fracture. This is a reasonable approximation for very low porosity/permeability media, but in some fractured systems, such as clays, significant interphase mass transfer from the entrapped phase may occur from regions of the interfaces that are coincident with the fracture matrix boundary [e.g., *O'Hara et al.*, 2000; *Parker et al.*, 1997]. Under these conditions, determining the relative rates of mass transfer by direct diffusion into the porous matrix and mass transfer into the fluid flowing through the fractures becomes important to understanding the long-term fate of an entrapped nonaqueous phase such as DNAPLs or CO_2. The continuum model presented here provides a robust approach for quantifying rates of mass transfer into the fracture fluid by advection and diffusion that can be directly compared to estimates of mass transfer by matrix diffusion alone. Furthermore, the ability of the continuum model to successfully predict mass transfer into the flowing phase in the fracture supports extending our modeling approach to directly include the influence of diffusive mass transfer into the porous matrix.

Appendix A

[46] As discussed in section 2, the depth-averaged flow and transport equations used to simulate mass transfer require simplifying assumptions that may influence local mass transfer calculations. To explore the sensitivity of mass transfer calculations to these simplifications, we consider calculations of mass transfer from the edges of a thin rectangular duct (Figure A1) with width, a, height (aperture), b and mass transfer from the edges at $z = -a/2$, $a/2$, which represent idealized fluid-fluid interfaces. Though this is a simplification of the geometry in the variable aperture fractures, where surface roughness creates both aperture variability and in-plane curvature of the fluid-fluid interfaces, it provides the ability to directly quantify the relative influence of velocity and concentration gradients that result from approximations to the velocity field in the vicinity of the fluid-fluid interface (i.e., $z = -a/2$, $a/2$). We consider three cases: (1) zero velocity on the fracture surfaces ($y = -b/2$, $b/2$) and at the fluid-fluid interfaces; (2) zero velocity on the fracture surfaces and zero shear on the edges of the duct; and (3) uniform velocity throughout the duct. Case 1 represents an extreme scenario, which is an approximate representation of an entrapped fluid with a much higher viscosity than the flowing fluid, though even for large viscosity contrasts, momentum transfer between the fluids will lead to a nonzero velocity at the interface. Case 2 represents an entrapped fluid with a similar or lower viscosity than the flowing fluid, resulting in negligible impact on velocities at the interface. Case 3 is identical to the approximations used by our depth-averaged mass transfer model.

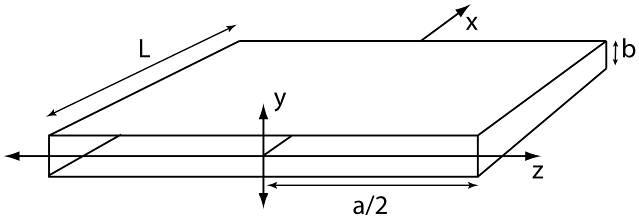

Figure A1. Schematic of geometry used for mass transfer calculations in an idealized geometry with three different velocity fields. Mass transfer occurs from the walls at $z = a/2$, $-a/2$, and flow is parallel to the x axis.

[47] We use a simplified approximation to the analytical solution for flow through a rectangular duct [e.g., *Kakaç et al.*, 1987] to represent the velocities for case 1:

$$\frac{u}{u_{\max}} = \left[1 - \left(\frac{y}{b}\right)^n\right]\left[1 - \left(\frac{z}{a}\right)^m\right]; \; \frac{u_{\max}}{u_m} = \left(\frac{m+1}{m}\right)\left(\frac{n+1}{n}\right)$$
$$m = 1.7 + 0.5(b/a)^{-1.4}$$
$$n = \begin{cases} 2 & \text{for } b/a \le 1/3 \\ 2 + 0.3(b/a - 1/3) & \text{for } b/a > 1/3 \end{cases} \tag{A1}$$

which results in estimates of velocity that differ by less than 1% from the exact analytical solution for Stokes flow in this geometry. For case 2, we assume the two fluids have similar viscosities (i.e., full slip condition at $z = -a/2$, $a/2$), which leads to a simplification of the velocity field:

$$\frac{u}{u_{\max}} = \left[1 - \left(\frac{y}{b}\right)^2\right]; \; \frac{u_{\max}}{u_m} = \frac{3}{2} \tag{A2}$$

To calculate steady state mass transfer from the fluid-fluid interfaces in each of the three cases, we used a finite difference discretization of the three-dimensional advection-diffusion equation:

$$\mathbf{u} \cdot \nabla c - \nabla \cdot (\mathbf{D} \cdot \nabla c) = 0; \; c = c_s \quad \text{for } z = -a/2, z = a/2 \tag{A3}$$

with mass transfer from the interface quantified as

$$j = D\frac{\partial C}{\partial z} = k(c_s - c_{in}) \quad \text{at } z = -a/2 \text{ and } a/2 \tag{A4}$$

To ensure sufficient resolution of the velocity fields and minimize the effects of numerical dispersion, the simulation used a grid spacing of $b/40$ and values of a such that $b/a = 0.1$ and 1. To compare results from the different simulations, we calculated the average dimensionless Sherwood number for each simulation:

$$\langle Sh \rangle = \frac{1}{A}\int_0^L \int_{-b/2}^{b/2} \frac{ky}{D_m} dxdy \tag{A5}$$

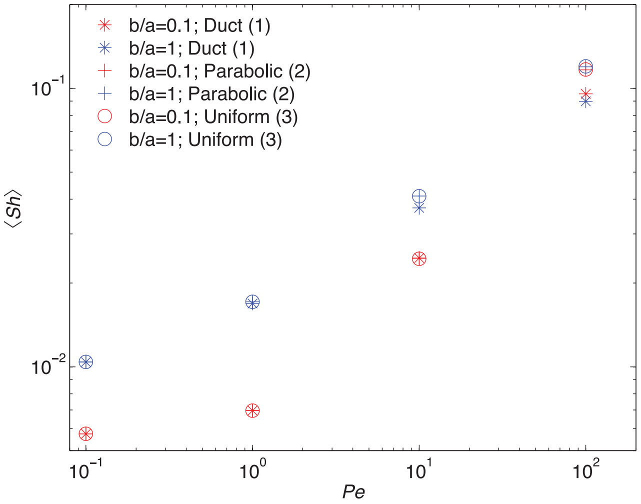

Figure A2. Average Sh plotted against Pe for three different approximations to the velocity field in a rectangular duct for two different aspect ratios.

which provides a measure of the total mass transfer for each simulation. Mass transfer simulations for values of $Pe = u_m b/D_m$ ranging from 0.1 to 100 demonstrate the influence of local differences in the velocity field in the vicinity of the interface on mass transfer rates (Figure A2). For small values of Pe, all three cases yield indistinguishable values of $\langle Sh \rangle$. However, at larger values of Pe ($Pe = 10$ for $b/a = 1$ and $Pe = 100$ for $b/a = 0.1$) the reduced velocities near the interface resulting from the no-slip boundary condition in the case 1 simulations leads to decreased mass transfer. When we assume that the fluid-fluid interface has a negligible influence on the velocity field near the interface (i.e., case 2), the mass transfer rates are insensitive to the presence or absences of a parabolic velocity profile across the fracture aperture for the range of Pe explored here. Because it is likely that momentum transfer across the fluid-fluid interface will lead to nonzero velocities at the interface, it is reasonable to assume that case 2 provides a simplified representation of the conditions in fractures occupied by regions of an entrapped dissolving fluid. Thus, the results presented here suggest that the simplifications resulting from depth averaging the flow and transport equations lead to negligible overestimations of local mass transfer rates. These observations are further supported by the excellent agreement demonstrated in our previously published comparison between experiment and simulation [*Detwiler et al.*, 2001].

[48] **Acknowledgments.** This work was performed with funding from the U.S. Department of Energy, Office of Basic Energy Sciences, Geosciences Program under contracts DE-FG02-09ER16003 (University of California, Irvine), DE-FG03-96ER14590 (University of Colorado at Boulder), and DE-AC04-94AL85000 (Sandia National Laboratories). This is contribution 40 from the Urban Water Research Center at University of California, Irvine.

References

Becker, M. W., M. Pelc, R. V. Mazurchuk, and J. Spernyak (2003), Magnetic resonance imaging of dense and light non-aqueous phase liquid in a rock fracture, *Geophys. Res. Lett.*, *30*(12), 1646, doi:10.1029/2003GL017375.

Brown, S. R. (1995), Simple mathematical-model of a rough fracture, *J. Geophys. Res.*, *100*(B4), 5941–5952, doi:10.1029/94JB03262.

Brusseau, M. L., H. Janousek, A. Murao, and G. Schnaar (2008), Synchrotron X-ray microtomography and interfacial partitioning tracer test measurements of NAPL-water interfacial areas, *Water Resour. Res.*, *44*(1), W01411, doi:10.1029/2006WR005517.

Chandler, R., J. Koplik, K. Lerman, and J. F. Willemsen (1982), Capillary displacement and percolation in porous-media, *J. Fluid Mech.*, *119*, 249–267.

Chomsurin, C., and C. J. Werth (2003), Analysis of pore-scale nonaqueous phase liquid dissolution in etched silicon pore networks, *Water Resour. Res.*, *39*(9), 1265, doi:10.1029/2002WR001643.

Culligan, K. A., D. Wildenschild, B. S. B. Christensen, W. G. Gray, and M. L. Rivers (2006), Pore-scale characteristics of multiphase flow in porous media: A comparison of air-water and oil-water experiments, *Adv. Water Resour.*, *29*(2), 227–238, doi:10.1016/j.advwatres.2005.03.021.

Detwiler, R. L., H. Rajaram, and R. J. Glass (2001), Nonaqueous phase liquid dissolution in variable aperture fractures: Development of a depth-averaged computational model with comparison to a physical experiment, *Water Resour. Res.*, *37*(12), 3115–3129, doi:10.1029/2000WR000161.

Detwiler, R. L., H. Rajaram, and R. J. Glass (2002), Experimental and simulated solute transport in a partially saturated, variable-aperture fracture, *Geophys. Res. Lett.*, *29*(8), 1272, doi:10.1029/2001GL013508.

Detwiler, R. L., H. Rajaram, and R. J. Glass (2005), Satiated relative permeability of variable aperture fractures, *Phys. Rev. E*, *71*, 031114, doi:10.1103/PhysRevE.71.031114.

Dickson, S. E., and N. R. Thomson (2003), Dissolution of entrapped DNAPLs in variable aperture fractures: Experimental data and empirical model, *Environ. Sci. Technol.*, *37*(18), 4128–4137, doi:10.1021/es026275r.

Dillard, L. A., and M. J. Blunt (2000), Development of a pore network simulation model to study nonaqueous phase liquid dissolution, *Water Resour. Res.*, *36*(2), 439–454, doi:10.1029/1999WR900301.

Glass, R. J., and M. J. Nicholl (1995), Quantitative Visualization of Entrapped Phase Dissolution within a Horizontal Flowing Fracture, *Geophys. Res. Lett.*, *22*(11), 1413–1416, doi:10.1029/95GL01491.

Glass, R. J., and L. Yarrington (2003), Mechanistic modeling of fingering, nonmonotonicity, fragmentation, and pulsation within gravity/buoyant destabilized two-phase/unsaturated flow, *Water Resour. Res.*, *39*(3), 1058, doi:10.1029/2002WR001542.

Glass, R. J., M. J. Nicholl, and L. Yarrington (1998), A modified invasion percolation model for low-capillary number immiscible displacements in horizontal rough-walled fractures: Influence of local in-plane curvature, *Water Resour. Res.*, *34*(12), 3215–3234, doi:10.1029/98WR02224. (Correction, *Water Resour. Res.*, *36*(7), 1991, doi:10.1029/2000WR900060, 2000.)

Glass, R. J., H. Rajaram, and R. L. Detwiler (2003), Immiscible displacements in rough-walled fractures: Competition between roughening by random aperture variations and smoothing by in-plane curvature, *Phys. Rev. E*, *68*, 061110, doi:10.1103/PhysRevE.68.061110.

Ji, S. H., M. J. Nicholl, R. J. Glass, and K. K. Lee (2004), Influence of a simple fracture intersection on density-driven immiscible flow: Wetting vs. nonwetting flows, *Geophys. Res. Lett.*, *31*(14), L14501, doi:10.1029/2004GL020045.

Jia, C., K. Shing, and Y. C. Yortsos (1999), Visualization and simulation of non-aqueous phase liquids solubilization in pore networks, *J. Contam. Hydrol.*, *35*(4), 363–387, doi:10.1016/S0169-7722(98)00102-8.

Johns, M. L., and L. F. Gladden (1999), Magnetic resonance imaging study of the dissolution kinetics of octanol in porous media, *J. Colloid Interface Sci.*, *210*(2), 261–270, doi:10.1006/jcis.1998.5950.

Kakaç, S., R. K. Shah, and W. Aung (1987), *Handbook of Single-Phase Convective Heat Transfer*, John Wiley, New York.

Kennedy, C. A., and W. C. Lennox (1997), A pore-scale investigation of mass transport from dissolving DNAPL droplets, *J. Contam. Hydrol.*, *24*(3–4), 221–246, doi:10.1016/S0169-7722(96)00011-3.

Knutson, C. E., C. J. Werth, and A. J. Valocchi (2001), Pore-scale modeling of dissolution from variably distributed nonaqueous phase liquid blobs, *Water Resour. Res.*, *37*(12), 2951–2963, doi:10.1029/2001WR000587.

Kueper, B. H., and D. B. Mcwhorter (1991), The behavior of dense, nonaqueous phase liquids in fractured clay and rock, *Ground Water*, *29*(5), 716–728.

Longino, B. L., and B. H. Kueper (1999), Nonwetting phase retention and mobilization in rock fractures, *Water Resour. Res.*, *35*(7), 2085–2093, doi:10.1029/1999WR900100.

Mahadevan, J., M. M. Sharma, and Y. C. Yortsos (2007), Water removal from porous media by gas injection: Experiments and simulation, *Transp. Porous Media*, *66*(3), 287–309.

Mayer, A. S., and C. T. Miller (1996), The influence of mass transfer characteristics and porous media heterogeneity on nonaqueous phase dissolution, *Water Resour. Res.*, *32*(6), 1551–1567, doi:10.1029/96WR00291.

Miller, C. T., M. M. Poirier-McNeill, and A. S. Mayer (1990), Dissolution of trapped nonaqueous phase liquids: Mass transfer characteristics, *Water Resour. Res.*, *26*(11), 2783–2796.

Nicholl, M. J., and R. J. Glass (2005), Infiltration into an analog fracture: Experimental observations of gravity-driven fingering, *Vadose Zone J.*, *4*(4), 1123–1151.

O'Hara, S. K., B. L. Parker, P. R. Jorgensen, and J. A. Cherry (2000), Trichloroethene DNAPL flow and mass distribution in naturally fractured clay: Evidence of aperture variability, *Water Resour. Res.*, *36*(1), 135–147, doi:10.1029/1999WR900212.

Or, D., and M. Tuller (2000), Flow in unsaturated fractured porous media: Hydraulic conductivity of rough surfaces, *Water Resour. Res.*, *36*(5), 1165–1177, doi:10.1029/2000WR900020.

Pan, C., E. Dalla, D. Franzosi, and C. T. Miller (2007), Pore-scale simulation of entrapped non-aqueous phase liquid dissolution, *Adv. Water Resour.*, *30*(3), 623–640, doi:10.1016/j.advwatres.2006.03.009.

Parker, B. L., R. W. Gillham, and J. A. Cherry (1994), Diffusive disappearance of immiscible-phase organic liquids in fractured geologic media, *Ground Water*, *32*(5), 805–820.

Parker, B. L., D. B. McWhorter, and J. A. Cherry (1997), Diffusive loss of non-aqueous phase organic solvents from idealized fracture networks in geologic media, *Ground Water*, *35*(6), 1077–1088, doi:10.1111/j.1745-6584.1997.tb00180.x.

Powers, S. E., L. M. Abriola, and W. J. Weber (1994), An experimental investigation of nonaqueous phase liquid dissolution in saturated subsurface systems: Transient mass transfer rates, *Water Resour. Res.*, *30*(2), 321–332, doi:10.1029/93WR02923.

Schnaar, G., and M. L. Brusseau (2005), Pore-scale characterization of organic immiscible-liquid morphology in natural porous media using synchrotron X-ray microtomography, *Environ. Sci. Technol.*, *39*(21), 8403–8410, doi:10.1021/es0508370.

Tokunaga, T. K., and J. M. Wan (1997), Water film flow along fracture surfaces of porous rock, *Water Resour. Res.*, *33*(6), 1287–1295, doi:10.1029/97WR00473.

Wilkinson, D., and J. F. Willemsen (1983), Invasion percolation: A new form of percolation theory, *Journal Physics A Math. Gen.*, *16*(14), 3365–3376.

Xu, B., Y. C. Yortsos, and D. Salin (1998), Invasion percolation with viscous forces, *Phys. Rev. E*, *57*, 739–751, doi:10.1103/PhysRevE.57.739.

Yang, D. Y., P. Tontiwachwuthikul, and Y. G. Gu (2005), Interfacial interactions between reservoir brine and CO2 at high pressures and elevated temperatures, *Energy Fuels*, *19*(1), 216–223.

Zhang, C. Y., C. J. Werth, and A. G. Webb (2002), A magnetic resonance imaging study of dense nonaqueous phase liquid dissolution from angular porous media, *Environ. Sci. Technol.*, *36*(15), 3310–3317, doi:10.1021/es011497v.

R. L. Detwiler, Department of Civil and Environmental Engineering, University of California, Irvine, CA 92697, USA. (detwiler@uci.edu)

R. J. Glass, Sandia National Laboratories, P.O. Box 5800, Albuquerque, NM 87185, USA.

H. Rajaram, Department of Civil, Environmental, and Architectural Engineering, University of Colorado at Boulder, Boulder, CO 80309, USA.